Geophysical Journal International

*Geophys. J. Int.* (2014) **198,** 775–794
Advance Access publication 2014 June 4
GJI Marine geosciences and applied geophysics

doi: 10.1093/gji/ggu161

# Inversion of airborne tensor VLF data using integral equations

Jochen Kamm[1] and Laust B. Pedersen[1,2]

[1]*Department of Earth Science, Uppsala University, Sweden. E-mail: jochen.kamm@geo.uu.se*
[2]*Geological Survey of Sweden, Uppsala, Sweden*

Accepted 2014 April 29. Received 2014 April 29; in original form 2013 November 7

## SUMMARY

The Geological Survey of Sweden has been collecting airborne tensor very low frequency data (VLF) over several decades, covering large parts of the country. The data has been an invaluable source of information for identifying conductive structures that can among other things be related to water-filled fault zones, wet sediments that fill valleys or ore mineralizations. Because the method only uses two differently polarized plane waves of very similar frequency, vertical resolution is low and interpretation is in most cases limited to maps that are directly derived from the data. Occasionally, 2-D inversion is carried out along selected profiles. In this paper, we present for the first time a 3-D inversion for tensor VLF data in order to further increase the usefulness of the data set. The inversion is performed using a non-linear conjugate gradient scheme (Polak-Ribière) with an inexact line-search. The gradient is obtained by an algebraic adjoint method that requires one additional forward calculation involving the adjoint system matrix. The forward modelling is based on integral equations with an analytic formulation of the half-space Green's tensor. It avoids typically required Hankel transforms and is particularly amenable to singularity removal prior to the numerical integration over the volume elements. The system is solved iteratively, thus avoiding construction and storage of the dense system matrix. By using fast 3-D Fourier transforms on nested grids, subsequently farther away interactions are represented with less detail and therefore with less computational effort, enabling us to bridge the gap between the relatively short wavelengths of the fields (tens of metres) and the large model dimensions (several square kilometres). We find that the approximation of the fields can be off by several per cent, yet the transfer functions in the air are practically unaffected. We verify our code using synthetic calculations from well-established 2-D methods, and trade modelling accuracy off against computational effort in order to keep the inversion feasible in both respects. Our compromise is to limit the permissible resistivity to not fall below 100 Ωm to maintain computational domains as large as $10 \times 10$ km$^2$ and computation times on the order of a few hours on standard PCs. We investigate the effect of possible local violations of these limits. Even though the conductivity magnitude can then not be recovered correctly, we do not observe any structural artefacts related to this in our tests. We invert a data set from northern Sweden, where we find an excellent agreement of known geological features, such as contacts or fault zones, with elongated conductive structures, while high resistivity is encountered in probably less disturbed geology, often related to topographic highs, which have survived predominantly glacial erosion processes. As expected from synthetic studies, the resolution is laterally high, but vertically limited down to the top of conductive structures.

**Key words:** Numerical solutions; Inverse theory; Numerical approximations and analysis; Electrical properties; Electromagnetic theory.

## 1 INTRODUCTION

The Swedish Geological survey (SGU) has been collecting tensor very low frequency (VLF) data over several decades. Nowadays, the data set covers Sweden almost entirely. Most commonly, the data is used in a qualitative way, in order to identify conductive and resistive zones in the upper few hundred metres of the crust. The typical situation in Sweden is a highly resistive crystalline basement.

Conductors therein are often associated with water-filled fracture zones, deformation zones, wet sediments that fill valleys and ore mineralizations.

Due to the dense spatial sampling (about 20 m along flight lines, 100–200 m between flight lines), detailed maps can be derived from the data set. Often, the so-called Peaker is displayed [horizontal divergence of magnetic transfer functions, Pedersen *et al.* (1994)] or, using a simple transformation introduced by Becken & Pedersen (2003), apparent resistivity and phase maps.

Quantitative interpretation is only carried out punctually (Oskooi & Pedersen 2005; Pedersen *et al.* 2009), using 2-D inversion routines developed for magnetotelluric data (Siripunvaraporn & Egbert 2000). Diffusive electromagnetic methods often exploit that the skin effect is a function of field frequency. It thus provides a means to differentiate current systems at different depth levels. Since usually only single-frequency transfer functions are extracted from the VLF band, vertical resolution is limited. While the top and the lateral position of conductors is relatively well defined, its actual conductivity as well its depth extent is not well determined.

On modern computer systems, large-scale 3-D inversion is becoming more common (Mackie & Madden 1993; Alumbaugh & Newman 1997; Newman & Alumbaugh 1997, 2000; Sasaki 2001; Siripunvaraporn *et al.* 2005; Cox *et al.* 2010; Zhdanov *et al.* 2010). Several contributions are dedicated to magnetic field transfer function inversion (Siripunvaraporn & Egbert 2009; Holtham & Oldenburg 2010, 2012). A 3-D inversion of single-transmitter VLF data using a block-model parametrized with 11 parameters was presented by Kaikkonen *et al.* (2012).

In this paper, we attempt for the first time the 3-D inversion of VLF airborne data on a large scale. First, we describe the general inversion methodology. Then we review the integral equation method in the context of airborne inversion and describe the approaches we employ, most of which are well known. We also present a novel nested variant of the common fast Fourier transform (FFT)-based approach for forward and adjoint modelling and give some insights for extracting the singularity from Green's tensor for the specific case of a homogeneous half-space background.

Next, we discuss the impact of topography on VLF anomalies. Eventually, we apply the inversion to synthetic pseudo 3-D data and a field example from Lappland, northern Sweden.

Despite the limitation to a single frequency and the ill-posedness of the inverse problem, we demonstrate that additional geometrical information can be uncovered through inversion, especially related to the top of conductive structures.

## 2 TENSOR VLF DATA

The frequency band 14–30 kHz is commonly referred to as the VLF band. The European continent is covered by a number of transmitters using the VLF band for submarine communications. Those transmitters act as remote sources that are exploited in the VLF method. Single-transmitter VLF maps have been produced by SGU since the 1960s. The tensor VLF concept (using different transmitters to measure independent source polarizations) was introduced in the 1980s. A detailed description of this technology was given by Pedersen *et al.* (1994). As in magnetotellurics, the VLF signal from distant transmitters can be treated as a plane wave and vertical magnetic transfer functions $T_{\{x,y\}}$ can be defined through the relation (Vozoff 1972)

$$H_z = T_x H_x + T_y H_y. \tag{1}$$

Here, $H_{\{x,y,z\}}$ are magnetic field components as functions of frequency. The transfer functions can be estimated from at least two different transmitters at sufficiently similar frequency. They are often referred to as the components of the 'Tipper' vector $\mathbf{t}$.

## 3 SOLUTION TO THE INVERSE PROBLEM

We present the electromagnetic inverse problem in the usual way as a minimization problem

$$\min_{\mathbf{m}} \Phi(\mathbf{m})$$

$$\Phi(\mathbf{m}) = \Phi_d(\mathbf{m}) + \beta \Phi_m(\mathbf{m}), \tag{2}$$

where the objective functional $\Phi$ is a combination of the data misfit $\Phi_d$ and a measure $\Phi_m$ of the structure in the model, weighted by the regularization parameter $\beta$. The former term is defined to measure the difference between the observations $\mathbf{d}^{\text{obs}}$ and the predictions $\mathbf{d}^{\text{pre}}$ from a model $\mathbf{m}$, namely

$$\Phi_d = \left\| \mathbf{C}_d^{-1/2} \left( \mathbf{d}^{\text{obs}} - \mathbf{d}^{\text{pre}} \right) \right\|_2^2. \tag{3}$$

The data vectors $\mathbf{d}$ contain both Tipper components, that is $\mathbf{d} = \left[ \mathbf{t}_x^T \ \mathbf{t}_y^T \right]^T$ where the entries of $\mathbf{t}_{\{x,y\}}$ are $t_{\{x,y\},i} = T_{\{x,y\}}(\mathbf{r}_i)$. The operator $\| \cdot \|_2$ denotes the L2-norm. The measurement inaccuracy is encoded in the data covariance matrix $\mathbf{C}_d$. Because there is no evidence to the contrary, we assume that the measurements are statistically independent, so that only the matrix diagonal holds elements different from zero, that is estimates of the data variance $\sigma_d^2$. Furthermore, since VLF measurements are very homogeneous, we only estimate a single value for either the whole data set or for each of the two tipper components $\mathbf{t}_{\{x,y\}}$. The predictions are obtained from a forward calculation denoted as $\mathbf{d}^{\text{pre}} = \mathbf{g}(\mathbf{m})$, which will be explained in detail later on (Section 4 and appendices). In order to construct the model vector $\mathbf{m}$, the domain of the inverse problem is decomposed into blocks of constant anomalous conductivity and of uniform lateral extent. Due to the diminishing resolution with depth, the vertical block size is increased by a factor of two from each layer to the next. To ensure that the conductivity values remain within the predefined boundaries $lb < \sigma_i < ub$, while simultaneously maintaining the unconstrainedness of problem (2), the open interval is transformed to unbounded variables $m_i$ using a well-known logarithmic parameter transform (e.g. Newman & Alumbaugh 2000)

$$m_i = \log_{10}(ub - \sigma_i) - \log_{10}(\sigma_i - lb). \tag{4}$$

The latter term in eq. (2) is necessary to deal with the non-uniqueness of the inverse problem by adding a minimum structure requirement to the model (e.g. Constable *et al.* 1987). In particular, we select a first difference linear operator $\mathbf{L}$. Then

$$\Phi_m = \|\mathbf{L}\mathbf{m}\|_2^2. \tag{5}$$

The regularization parameter $\beta$ is selected by trial and error. A good starting point is

$$\beta^* = \frac{\Phi_d(\mathbf{m}_0)}{M}, \tag{6}$$

where $\mathbf{m}_0$ is the starting model and $M$ the number model parameters. This rule of thumb is obtained from balancing $\Phi_d(\mathbf{m}_0)$ with $\Phi_m$, the latter being crudely approximated as $M$. In our experience, a favourable value can usually be found in the interval $\frac{\beta^*}{10} < \beta < 10\beta^*$.

The inverse problem (2) is non-linear and must thus be solved iteratively. Iterations are stopped as soon as the desired data misfit $\Phi_d^* \approx N$ has been achieved. This criterion is often referred to as the discrepancy principle (e.g. Aster *et al.* 2005). The regularization parameter $\beta$ can be slightly decreased during the inversion (we choose a reduction factor of 0.7) if the convergence severely stalls ($\Phi_d$ stops decreasing) before the inversion target is reached.

We employ a non-linear conjugate gradient technique (NLCG; Polak & Ribière 1969; Zhdanov 2002; Nocedal & Wright 2006) with an inexact line-search. Non-linear conjugate gradients have been applied to 2-D and 3-D magnetotelluric inversion (Newman & Alumbaugh 2000; Rodi & Mackie 2001). We use an equivalent line-search like Newman & Alumbaugh (2000) have described.

The choice of a gradient based method is due to the relatively manageable computational requirements. One calculation of the gradient of the objective functional with respect to the model parameters, and a small number of forward computations during the line-search (typically only two) is required in one iteration. The gradient calculation is about as expensive as one forward calculation. We use an algebraic adjoint method for that, which is explained in Section 4.3 and Appendix E.

It is well known that such algorithms are easily outperformed by (Gauss-)Newton methods (Mackie & Madden 1993; Sasaki 2001; Grayver *et al.* 2013) in terms of iterations. However, Jacobian and (at least approximate) Hessian matrices need to be available, and both are very expensive to compute. At present, data fitting requirements are moderate, since measurements have limited accuracy. A candidate for a compromise between expensive (Gauss-)Newton methods and gradient descent techniques are the quasi-Gauss-Newton methods, which employ inexpensive low-rank approximations to the second derivatives (e.g. Avdeev & Avdeeva 2009).

All gradient descent algorithms iteratively update the model estimate along directions that are in some way constructed from the local gradient direction and proceed to at least a local minimum point within this 1-D subspace of the model space. The subproblem is referred to as line-search. If the update direction is simply the negative gradient direction in each iteration, the algorithm falls in the category of steepest descent algorithms. Because every subsequent model update can destroy the subspace optimality achieved in previous steps, these algorithms often follow a slow, possibly even oscillating convergence trajectory. However, a simple correction to the descent direction can be made to preserve the subspace optimality of the respective previous steps. The direction is modified to be 'conjugate' to previous directions, hence the name 'conjugate gradients'. All but the first descent directions are modified in NLCG. If the underlying equations are linear, the objective function is quadratic. In this case, the conjugacy is perfect and holds recursively for all steps taken in the past. For a non-linear problem, however, the correction may only work a few steps back. As a theoretical consequence, NLCG should be restarted from time to time with a steepest descent step. A further complication is the problem of finding the minimum along the search direction, which is only trivial for the quadratic of the linear problem. Commonly, it is stated that the advantage of conjugate gradient methods over simpler gradient descent techniques depends crucially on the accuracy of the line-search procedure (Nocedal & Wright 2006). If it is not sufficiently accurate, no optimality is achieved along the update direction in the first place, and the idea of preserving the subspace optimality apparently becomes meaningless. Rodi & Mackie (2001) argued that the algorithm requires a restart whenever the line-search procedure fails. Newman & Alumbaugh (2000) suggested to use an inexact line-search nevertheless, and follow the obtained directions as long as they are descent directions. While we agree with the theoretical argument, our practical experience suggests that for our application, where the solution that we seek is away from the theoretically attainable minimum due to noise and data bias, conjugate gradients with an inexact line-search work very well.

Note also that, like any other non-linearity, the variation of $\beta$ during the inversion destroys the conjugacy of previous update directions. This can be addressed by restarting the conjugate gradient sequence after changing $\beta$.

## 4 ELECTROMAGNETIC FORWARD MODEL USING INTEGRAL EQUATIONS

Here, we give a review of the integral equation technique as applied to the inverse problem at hand, which, together with the appendices, should allow others to reproduce our work. Most of the material presented below has been published before by other authors. We also introduce a nested FFT technique to rapidly approximate relevant matrix-vector products.

### 4.1 Solution of the integral equation

#### *4.1.1 Integral equation formulation*

This following explanations have already been stated by Weidelt (1975), Raiche (1974), Hohmann (1975), Wannamaker *et al.* (1984) and Avdeev *et al.* (1997) in different ways. We give only a short summary here in order to establish the notation and the context.

In this description, the Earth is assumed to be planar, free of topography and non-magnetic (the magnetic permeability $\mu$ takes the vacuum value $\mu_0$ everywhere). These are typical simplifications in magnetotelluric modelling. The most problematic of them is the topography assumption. Further below (Section 5), we provide an investigation of topography effects. All fields have $\exp(i\omega t)$ time dependency ($\omega = 2\pi f$, with frequency $f$). Moreover, for frequencies and conductivities in the range of the VLF application the quasi-static approximation is not strictly valid, but displacement currents can be neglected with only minor consequences that are well within data uncertainties (Kalscheuer *et al.* 2008). The volume integral formulations rely on an abstract decomposition of the conductivity structure

$$\sigma(\mathbf{r}) = \sigma_b(\mathbf{r}) + \sigma_a(\mathbf{r}) \tag{7}$$

into a background component $\sigma_b$ and the deviation there-from, the so-called anomalous conductivity $\sigma_a$. Then, the electric and magnetic field pair $\mathbf{E}$ and $\mathbf{H}$ occurring in $\sigma$ also decomposes into

$$\begin{aligned} \mathbf{E} &= \mathbf{E}_p + \mathbf{E}_s \\ \mathbf{H} &= \mathbf{H}_p + \mathbf{H}_s. \end{aligned} \tag{8}$$

The primary fields $\mathbf{E}_p$ and $\mathbf{H}_p$ are the fields occurring in background structure $\sigma_b$ due to an external source. By choosing an appropriately simple $\sigma_b$, calculation of the primary fields is made comparatively easy. As it will be discussed later in detail, we select a homogeneous half-space wherein primary fields are given in closed form for many common source types. The secondary fields $\mathbf{E}_s$ and $\mathbf{H}_s$ originate from the interaction of the primary fields with the anomalous conductivity. Following largely the notation proposed

by Weidelt (1975), we define the wave numbers

$$k^2 = \mathrm{i}\omega\mu\sigma$$

$$k^2_{\{a,b\}} = \mathrm{i}\omega\mu\sigma_{\{a,b\}}. \tag{9}$$

The integral equation which is satisfied by the electric field reads then

$$\mathbf{E}(\mathbf{r})\cdot\hat{\mathbf{u}}_i = \mathbf{E}_p(\mathbf{r})\cdot\hat{\mathbf{u}}_i - \sum_{j=x,y,z}\int_{V'}\left(\mathbf{G}_j(\mathbf{r}'|\mathbf{r})\cdot\hat{\mathbf{u}}_i\right)k_a^2(\mathbf{r}')\left(\mathbf{E}(\mathbf{r}')\cdot\hat{\mathbf{u}}_j\right)\mathrm{d}V' \tag{10}$$

where $i, j = x, y, z$. The vectors $\hat{\mathbf{u}}_i$ are unit vectors pointing along the $i$-direction. The Green's vectors

$$\mathbf{G}_j = \left[\, G_{jx}\;\; G_{jy}\;\; G_{jz}\,\right]^T \tag{11}$$

are electric fields at $\mathbf{r}$ due to an $j$-directed electric unit dipole located at $\mathbf{r}'$ in $\sigma_b$. More specifically, they are solutions to the particular diffusion equation

$$\nabla\times\nabla\times\mathbf{G}_j(\mathbf{r}'|\mathbf{r}) + k_b^2(\mathbf{r})\mathbf{G}_j(\mathbf{r}'|\mathbf{r}) = \delta(\mathbf{r}-\mathbf{r}')\hat{\mathbf{u}}_j \tag{12}$$

where $\delta(\mathbf{r})$ is the 3-D Dirac delta. The $G_{ij}$ are also the elements of Green's tensor. The dot product is defined as

$$\mathbf{a}\cdot\mathbf{b} = \sum_i a_i b_i. \tag{13}$$

It is symmetric, but not Hermitian ($\mathbf{a}\cdot\mathbf{a}$ is not always real-valued).

Since the integral on the right-hand side only has contributions to $\mathbf{E}(\mathbf{r})$ where $\sigma_a(\mathbf{r}')$ is non-zero, the electric field is completely determined, once the solution of eq. (10) is known on the domain of the anomaly. For the electric fields at all other places, eq. (10) becomes explicit. Likewise, magnetic fields at any observer position $\mathbf{r}$ are obtained using the magnetic Green's tensor $\mathbf{M}$ corresponding to $\mathbf{G}$. It follows from Faraday's law

$$\nabla\times\mathbf{G}(\mathbf{r}'|\mathbf{r}) = -\mathrm{i}\omega\mu\mathbf{M}(\mathbf{r}'|\mathbf{r}) \tag{14}$$

where the curl operator acts on the $\mathbf{r}$-coordinate. Then

$$\mathbf{H}(\mathbf{r})\cdot\hat{\mathbf{u}}_i = \mathbf{H}_p(\mathbf{r})\cdot\hat{\mathbf{u}}_i + \sum_{j=x,y,z}\int_{V'}\left[\mathbf{M}_j(\mathbf{r}'|\mathbf{r})\cdot\hat{\mathbf{u}}_i\right)k_a^2(\mathbf{r}')\left(\mathbf{E}(\mathbf{r}')\cdot\hat{\mathbf{u}}_j\right]\mathrm{d}V'. \tag{15}$$

In this study, the integral eqs (10) and (15) are discretized using rectangular blocks, within each of which the electric field as well as the ground conductivity are assumed constant. This technique has been used previously by for example Weidelt (1975) or Hohmann (1975). It is explained in detail in Appendix A, where we also give an exact description of the resulting column vectors and matrices. In essence, eq. (10) can be approximated by a linear system of equations

$$\mathbf{A}\mathbf{E} = \mathbf{E}_p, \tag{16}$$

where $\mathbf{E}$ and $\mathbf{E}_p$ are column vectors containing the discrete values of the total and the primary electric fields, respectively. Additionally, the system matrix $\mathbf{A}$ reads

$$\mathbf{A} = \mathbf{I} + \mathbf{K}\Sigma. \tag{17}$$

The matrix $\mathbf{I}$ is a unit matrix with dimensions corresponding to field discretization. The matrix $\Sigma$ is a diagonal matrix, which contains the anomalous conductivity values $k^2_{a,l}$ of the blocks $l$ on its diagonal.

The kernel matrix $\mathbf{K}$ holds the elements of Green's tensor, which are integrated over these blocks $l$ with volumes $V_l$, for all block midpoints $\mathbf{r}_k$, namely

$$\int_{V_l} G_{ij}(\mathbf{r}_k|\mathbf{r}')\mathrm{d}V'. \tag{18}$$

Due to the singular nature of the Green's tensor elements for $\mathbf{r}_k = \mathbf{r}'$, the numerical evaluation of the integrals is difficult, and deserves a separate discussion (Section 4.2.2 and Appendix C).

In analogy, eq. (15) for the magnetic fields is discretized as

$$\mathbf{H} = \mathbf{H}_p + \mathbf{K}_M\Sigma\mathbf{E}, \tag{19}$$

where $\mathbf{K}_M$ is the magnetic kernel matrix that contains volume integrals of the form (see Appendix A for details)

$$\int_{V_l} M_{ij}(\mathbf{r}_{\tilde{k}}|\mathbf{r}')\mathrm{d}V'. \tag{20}$$

The magnetic fields $\mathbf{H}$, $\mathbf{H_p}$ and the columns of $\mathbf{K}_M$ are discretized only at the measurement positions $\mathbf{r}_{\tilde{k}}$. The expressions for the magnetic Green's tensor are given in Appendix D.

Since it will be required later for the calculation of the gradient of the objective function (Section 4.3), we briefly state the discrete adjoint problem to eq. (16). The system (16) is not, as it is usual in electromagnetics, complex-symmetric, because the right-hand side represents a field quantity instead of a current source. The adjoint problem is thus

$$\mathbf{A}^\dagger\mathbf{u} = \mathbf{u}_p \tag{21}$$

for some adjoint source $\mathbf{u}_p$ and adjoint state $\mathbf{u}$. Here

$$\mathbf{A}^\dagger = \mathbf{I} + \Sigma^\dagger\mathbf{K}^\dagger = \mathbf{I} - \Sigma\mathbf{K}^\dagger$$

$$\left[\mathbf{K}^\dagger\right]_{mn} = \overline{K_{nm}}$$

$$\Sigma^\dagger = -\Sigma, \tag{22}$$

where $\overline{K}$ is the conjugate complex of $K$.

### 4.1.2 *Iterative solution and preconditioning*

The matrix $\mathbf{A}$ is dense and of dimension $3M\times 3M$, where $M$ is the number of blocks in the earth model. A direct solution that involves the inversion of $\mathbf{A}$ seems at present out of the question. Therefore, we choose to employ an iterative method that only requires matrix-vector products involving $\mathbf{A}$ or $\mathbf{A}^\dagger$ to find an approximate solution.

We have found that while occasionally, solutions are produced very rapidly with the stabilized bi-conjugate gradient method (BiCGstab), convergence does not always occur. In contrast, the generalized minimum residual method (GMRES) proves a steady, stable convergence behaviour, which is very predictable, but never surprisingly fast. In the context of the inverse problem, the anomaly can be arbitrary. Since GMRES performs largely independent of the particular model (apart from the fact that larger anomaly magnitudes require more iteration), we rely on it in our implementation.

To speed up the solution, we apply the contraction method (Avdeev *et al.* 1997) in the form given by Hursan & Zhdanov (2002). In this method, the linear system (16) is left- and right-preconditioned by two rapidly computed diagonal matrices. The cost for this is negligible, but the solution of the system is obtained in sometimes less than half the number of iterations as required without the preconditioning. The contraction method is especially beneficial when large conductivity contrasts occur and thus accelerates the costliest calculations most. It is important to notice that

when applying the method to the adjoint eqs (21), the adjoint of the preconditioner must be applied, which reverses the roles of the left- and right-preconditioning matrices.

#### *4.1.3 Matrix multiplications*

Products involving the matrices $\mathbf{A}$ and $\mathbf{A}^\dagger$ can be split up in multiplications involving the component matrices $\mathbf{I}$, $\Sigma$ and $\mathbf{K}$. The unit matrix $\mathbf{I}$ does not require any work and multiplying the diagonal matrix $\Sigma$ also comes at a negligible cost. The most expensive operation involves the electric kernel matrix $\mathbf{K}$ containing the Green's tensor's volume integrals. While it has no zero elements, it does contain a great deal of structure and redundancy, which especially surfaces when cast into components of block-Toeplitz-like form. Then the matrix can be multiplied with a vector using convolutions, which are efficiently carried out in wavenumber domain. In the literature, often horizontal wavenumber domain formulations are exploited, which rely on a horizontally invariant background medium (e.g. Avdeev *et al.* 1997; Tseng *et al.* 2003). Green's tensor is then also invariant against a horizontal translation of the source–receiver pair:

$$G_{ij}(x, y, z|x', y', z') = G_{ij}(0, 0, z|x' - x, y' - y, z'). \tag{23}$$

It has been demonstrated by Millard & Liu (2003) that in such a layered background medium, the Fourier transform can be applied to all three space dimensions. We apply their approach to our somewhat simpler situation of a homogeneous half-space background. Because the only inhomogeneity in $\sigma_b$ in vertical direction is the air–Earth interface, Green's tensor can be decomposed into direct waves and waves reflected from this interface:

$$\begin{aligned} G_{ij}(x, y, z|x', y', z') = {} & G^-_{ij}(0, 0, 0|x' - x, y' - y, z' - z) \\ & + G^+_{ij}(0, 0, 0|x' - x, y' - y, z' + z). \end{aligned} \tag{24}$$

The first term is invariant against any translation of the source–observer pair. The second term is invariant against the common translation of the observer and a virtual source located above the surface, which is the actual source mirrored at $z = 0$. The respective contributions are easily identified in the employed formulation of the Green's tensor (Section 4.2.1). In order to preserve the translation invariance for the discrete kernel $\mathbf{K}$, the discretization must be chosen uniform along all three space dimensions, so that all blocks have the edge lengths $\Delta_x$, $\Delta_y$ and $\Delta_z$. By splitting the integrands to the Green's tensor integrals according to the decomposition (24), we obtain $\mathbf{K}$ in terms of a sum of two matrices

$$\mathbf{K} = \mathbf{K}^- + \mathbf{K}^+, \tag{25}$$

whose elements are then invariant against discrete translation. Then, both $\mathbf{K}^+$ and $\mathbf{K}^-$ have a Toeplitz-like structure and their elements can be arranged as a convolution kernel on a 3-D grid. Thus, the two parts $\mathbf{K}^+\mathbf{f}$ and $\mathbf{K}^-\mathbf{f}$ of the product $\mathbf{Kf}$ of $\mathbf{K}$ with some vector $\mathbf{f}$ can be calculated separately via digital convolutions, which are evaluated using the 3-D FFT. A detailed description of the required operations, as well as the product involving the adjoint kernel $\mathbf{K}^\dagger$ is given in Appendix B. There, we also detail the matrix representation (expression B4) and the kernel representation for $\mathbf{K}^\pm$ (expressions B5 and B6).

#### *4.1.4 Approximate matrix products using nested FFTs*

Since the principal computational effort in the products involving the system matrix $\mathbf{A}$ or its adjoint $\mathbf{A}^\dagger$ are the products $\mathbf{Kf}$ and $\mathbf{K}^\dagger\mathbf{f}$, we describe here a method for specifically speeding up these operations.

The representation of the fields and conductivity on a uniform grid is a requirement for the use of FFTs. Green's tensor has steep slopes in the vicinity of the source. Therefore, for an accurate modelling using pulse basis functions, a fine discretization is required. On the other hand, the kernel becomes smooth rapidly with increased distance to the source.

This obstacle is for example tackled using pre-corrected FFTs as described by Phillips & White (1996). A more recent application in electromagnetic geophysics has been presented by Nie *et al.* (2013). A fine, usually unstructured grid is used only for close-range interactions, and far-range interactions are represented by proxy point dipoles located on the nodes of a uniform grid. The uniform part is then evaluated with FFTs similar as it has been described above. The term 'pre-corrected' refers to the necessity of correcting the input to the Fourier product by the interaction that has already been accounted for on the fine grid. We follow a similar, but simpler idea. Instead of a uniform grid together with a variable grid, we use several nested uniform block grids, applying only a certain range of the kernel on each grid. By using uniform grids, we can use FFTs throughout, and our counterpart of the pre-correction step becomes almost trivial.

We approximate $\mathbf{Kf}$ by the following procedure (see also the illustration given in Fig. 1): we separate $\mathbf{K}^\pm$ (also denoted as $\mathbf{L}^\pm_0$) into a short range part $\mathbf{K}^\pm_0$ and its long range complement $\mathbf{L}^\pm_0 - \mathbf{K}^\pm_0$. The subscript $j = 0$ indicates that all three quantities are represented on the finest grid. We keep the short range part and replace the complement by an approximation $\mathbf{L}^\pm_1$ on the next coarser scale grid ($j = 1$) by using localized spatial averages. Dropping the short-range part from $\mathbf{L}^\pm_1$ decreases its high wavenumber content considerably and thus permits down-sampling without significant loss of information. This removal is the counterpart to the pre-correction in the pre-corrected FFT method. The procedure is then repeated with $\mathbf{L}^\pm_1$, splitting it into an intermediate range part $\mathbf{K}^\pm_1$ and an approximation $\mathbf{L}^\pm_2$ to the remainder. We continue until $\mathbf{K}^\pm$ is completely decomposed. Then we compute a down-sampled version $\mathbf{f}_j$ for each scale, and apply the corresponding partial kernels $\mathbf{K}^\pm_j$ to it as described in

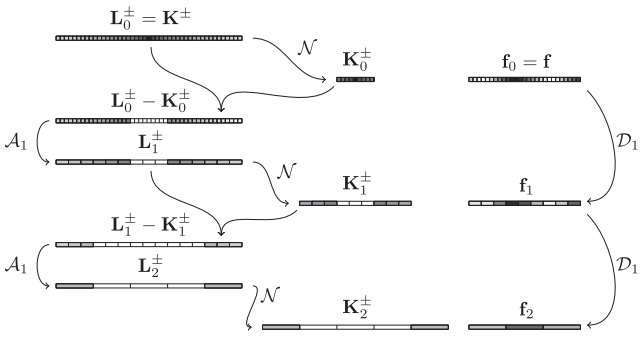


**Figure 1.** Left-hand panel: sketch of the generation process of the nested kernel matrices $\mathbf{K}^\pm_i$ from the original fine scale kernel $\mathbf{K}^\pm$ in one dimension and for three scales (see algorithm described in the text). The elements of the kernels are arranged as convolution kernels, with the source point in the centre. Dark colours indicate large values, white denotes zero. From top to bottom, the scale of the kernel becomes successively coarser. Right-hand panel: the sequence of down-sampled versions $\mathbf{f}_i$ generated successively from vector $\mathbf{f}$ in its original fine scale representation. After the generation of $\mathbf{K}_i$ and $\mathbf{f}_i$, the partial products $\mathbf{K}_i\mathbf{f}_i$ can be performed and their results are accumulated on the original fine scale.

Section 4.1.3 and Appendix B, and accumulate the partial sums to obtain an approximation to **Kf**.

For a detailed discussion of this, we may study the formalization of the algorithm:

$$\mathbf{L}_0^{\pm} = \mathbf{K}^{\pm}$$

$$j = 0, \tag{26}$$

then repeat

$$\mathbf{K}_j^{\pm} = \mathcal{N}\left\{\mathbf{L}_j^{\pm}\right\}$$

$$\mathbf{L}_{j+1}^{\pm} = \mathcal{A}_1\left\{\mathbf{L}_j^{\pm} - \mathbf{K}_j^{\pm}\right\}$$

$$j = j + 1 \tag{27}$$

until $jN^* \geq N_{\{x,y,z\}}$. After these preliminary steps, the product is evaluated by

$$\mathbf{f}_0 = \mathbf{f}$$

$$\mathbf{f}_{j+1} = \mathcal{D}_1\left\{\mathbf{f}_j\right\}$$

$$\mathbf{Kf} \approx \sum_j \mathcal{U}_j\left\{\mathbf{K}_j^{-}\mathbf{f}_j + \mathbf{K}_j^{+}\mathbf{f}_j\right\}. \tag{28}$$

The adjoint product $\mathbf{K}^{\dagger}\mathbf{f}$ can be obtained by replacing all occurrences of $\mathbf{K}^{\pm}$ with $(\mathbf{K}^{\pm})^{\dagger}$.

The operation of selecting a short-range subset is denoted as $\mathcal{N}\{\cdot\}$. For $\mathbf{L}_j^{-}$ all blocks closer to the source position than a certain distance are considered. In the case of $\mathbf{L}_j^{+}$, the relevant distance is to the mirror source. We represent the elements of $\mathbf{L}_j^{\pm}$ as convolution kernels, where they are gathered into a 3-D grid with the indices $k_x$, $k_y$, $k_z$ (i.e. the forms B5 and B6 in Appendix B). Then, we extract those elements for which $k_{\{x,y,z\}} \leq N^*$, where $N^*$ is defined as a fixed small number. The respective short-range distance for each nesting level is then proportional to the grid scale.

The operation $\mathcal{D}_1\{\cdot\}$ represents a spatial down-sampling of the argument by one scale by taking a local average. Each vector component is considered independently. Application of $\mathcal{D}_1$ to a field is straight-forward, as can be seen from a grid representation like (B3). Each average is computed over $p \times p \times p$ elements, reducing a $N_x \times N_y \times N_z$ grid to a $\frac{N_x}{p} \times \frac{N_y}{p} \times \frac{N_z}{p}$ grid.

The pseudo-inverse operator of $j$ consecutive applications of $\mathcal{D}_1$ is denoted as $\mathcal{U}_j\{\cdot\}$, up-sampling from any coarse grid to the original grid. It attributes the value of a large block to all small blocks inside it.

The operation $\mathcal{A}_1\{\cdot\}$ gives the approximation of a matrix argument by a corresponding matrix on the next coarser grid. The approximation can be carried out in different ways. It is natural to consider the arithmetic mean of the averaged matrix block, that is to apply $\mathcal{D}_1$ first to the columns and $p \cdot \mathcal{D}_1$ to the rows of the matrix. The factor $p$ is required because the row dimension represents volume integrals that must be summed instead of averaged. Alternatively, because all matrices are of Toeplitz-type, $\mathcal{A}_1$ can be defined simply as an averaging of the convolution kernel that comprises the matrix rows. This can be achieved through the application of $p \cdot \mathcal{D}_1$ to the kernel elements arranged in the form of a convolution kernel on a grid (expressions B5 or B6). The Toeplitz-type matrix obtained from the averaged kernel is not column averaged. Instead, each column contains only the entries that relate the averaged coarse scale volume elements to the midpoints of other coarse scale volume elements. While the former of two methods requires all finest grid matrix elements to be known and recursively builds coarser elements from them scale by scale, the elements in the latter method can be directly integrated, and are thus significantly less work. The first approximation is theoretically more justified because it is an approximation of the matrix instead of the kernel. However, our experiments show that the difference between both approximations is in fact much smaller than the error introduced by either of the two approximations. The reason is that the difference between two averages is on the order of the magnitude of the variation of the fine scale representation over the approximating large scale cell. In order to make the approximation feasible in the first place, the range parameter $N^*$ must be chosen large enough so that this variation is small. We choose to use the second method, which is much more economical.

Note, that while in the non-nested version of the algorithm, the size of the Fourier products $N_{\text{full}} = (3N_x - 2) \times (3N_y - 2) \times (3N_z - 2)$ (i.e. $N_{\{x,y,z\}}$ and $2N_{\{x,y,z\}} - 1$ elements along the respective dimensions of **f** and **K**) is reduced to $N_{\text{nested}} = (N_x + 2N^* - 2) \times (N_y + 2N^* - 2) \times (N_z + 2N^* - 2)$ on the finest scale, which comprises by far the most work intensive part. Since the range parameter $N^*$ is usually much smaller than $N_{\{x,y\}}$, it follows that $N_{\text{full}} \approx 9N_{\text{nested}}$. The computational effort of the Fourier transform is proportional to $N \log N$ (Cooley & Tukey 1965). Therefore, we expect that the ratio of computation times between the full and nested FFT keeps increasing by a logarithmic factor. Results of a performance test with variable horizontal model size are shown in Fig. 2. Because of the large memory requirements for the full FFT, we were only able to compare calculations up to slightly more than $10^5$ field variables. For small models, the improvement is as expected not significant. For larger models, the acceleration factor increases to ≈6.4 throughout the experiment, but the increase slows down, which is also in agreement with our expectations.

While the modelling accuracy is assessed in Section 4.4, the error that is exclusively caused by the approximate matrix product is illustrated in Figs 3 and 4. The secondary electric field for a

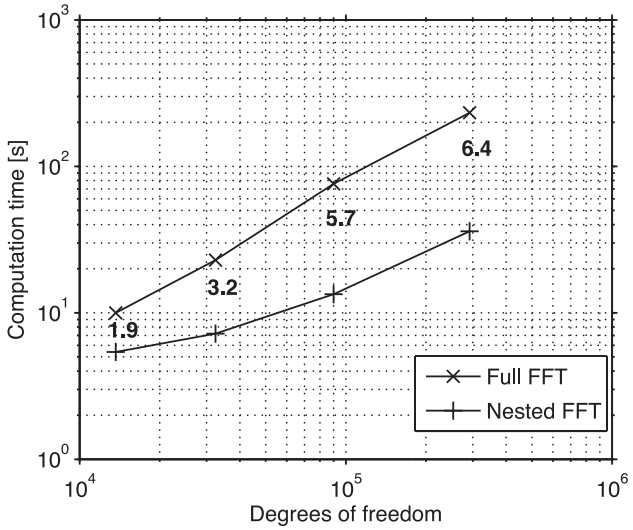


**Figure 2.** Comparison of computation time for both polarizations over degrees of freedom of the fields, using full FFT ('×') and the nested grid approximation ('+') for the matrix products. All measurements were taken from calculations without pre-conditioning. The anomalous domain consists of $N \times N \times 12$ blocks, that is, the number of parameters is varied along the horizontal dimensions. The bold numbers represent the speed-up ratio $\frac{t_{\text{full}}}{t_{\text{nested}}}$.

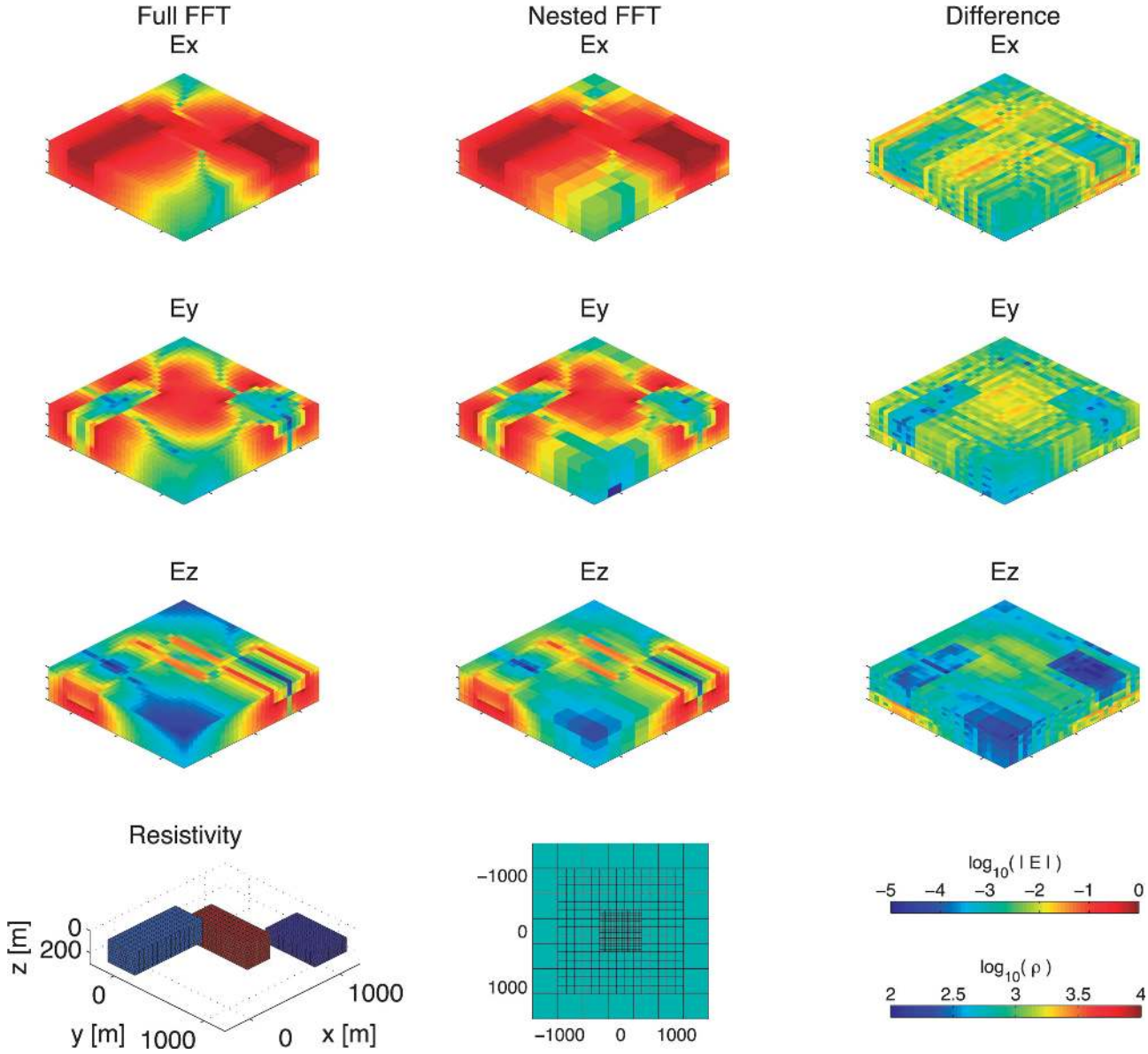


**Figure 3.** Absolute value of the secondary field due to an $E_x$—polarized plane wave computed on a fine grid (block size 50 m × 50 m × 25 m, left-hand column) and using the nested grid approximation (central column, grid displayed at the bottom). The right-hand column shows the magnitude of the difference between the full and the approximate modelling. The resistivity model used is displayed at the bottom left-hand side (background 5000 Ωm)

simple conductivity model (two conductive and a resistive block in a 5000 Ω-m background, see Fig. 3, bottom left) due to a plane wave $\mathbf{E_p} = \hat{\mathbf{u}}_x e^{-k_b^2(z)z}$ is modelled once on a fine grid and once using the nested grid approximation (Fig. 3, left-hand and central column). A horizontal slice through the nested grids is shown as well (Fig. 3, bottom central panel). The same nested grid is used throughout this study ($p = 3$ and $N^* = 7$, i.e. the edges of the subgrids consist of 15 blocks).

The approximation is most accurate within the anomalous bodies, but away from them the error in the fields due to the coarsening becomes evident. The overall error is 6 per cent for this example. While this is a significant error amplitude, the transfer functions at 60 m height over the model are practically unaffected by the approximation because the errors in the Earth are mostly high wavenumber features that are filtered out by the upward continuation to the measurement coordinates (compare Fig. 4).

## 4.2 Green's tensor

### *4.2.1 Definition and analytic expressions*

Green's vectors are defined as the solutions to

$$\nabla \times \nabla \times \mathbf{G}_i(\mathbf{r}'|\mathbf{r}) + k_b^2 \mathbf{G}_i(\mathbf{r}'|\mathbf{r}) = \delta(\mathbf{r} - \mathbf{r}')\hat{\mathbf{u}}_i. \quad (29)$$

Physically, they represent the electric field in a conductivity structure $\sigma_b(\mathbf{r})$ excited by a unit point dipole oriented along the $i$-direction, and located at $\mathbf{r}'$. Green's tensor is composed of the three Green's vectors for $i = x, y, z$.

For layered (only vertically varying, piecewise constant) $\sigma_b$, the equation is solved in the usual way by transforming it to horizontal wavenumber domain and finding the solution for every individual wavenumber analytically. The Fourier synthesis involves Hankel integrals of the obtained expressions. For the case of $\sigma_b$ representing a homogeneous half-space, closed-form integrals have been found

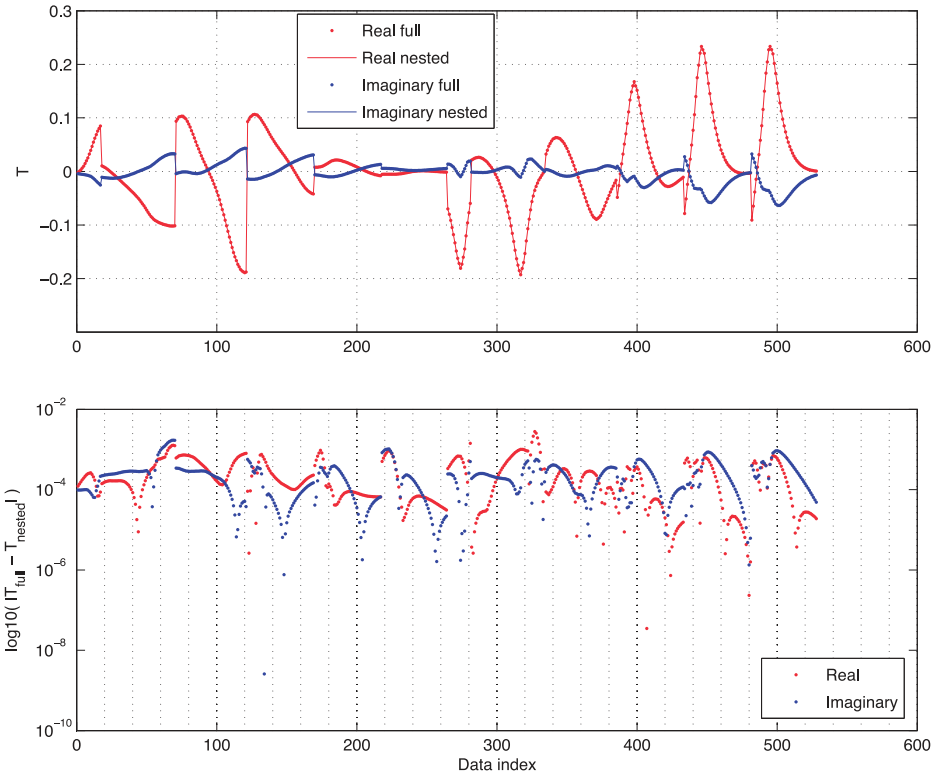


**Figure 4.** Top: transfer functions $T_{\{x,y\}}$ derived from the fields displayed in Fig. 3 at a flight height of 60 m. Dots: fine grid modelling. Solid line: nested grid approximation. Bottom: difference between the two. The transfer functions are ordered by their index in the data vector, which is of no particular importance here.

for both field and source located in the subsurface (Raiche 1975; Weidelt 1975). In our notation, with

$$R_{\pm}^2 = (x - x')^2 + (y - y')^2 + (z \pm z')^2 \tag{30}$$

$$g_{\pm} = \frac{\mathrm{e}^{-k_E R_{\pm}}}{4\pi R_{\pm}} \tag{31}$$

$$\gamma = \partial_z \left\{ I_0 \left[ \frac{1}{2} k_E \left( R_+ - z - z' \right) \right] K_0 \left[ \frac{1}{2} k_E \left( R_+ + z + z' \right) \right] \right\} / (2\pi) \tag{32}$$

the Green's tensor elements for $z > 0, z' > 0$ and for a conductivity structure

$$\sigma_b(z) = \begin{cases} 0 & z < 0 \\ \sigma_E & z > 0 \end{cases}$$

$$k_E^2 = \mathrm{i}\omega\mu\sigma_E \tag{33}$$

read

$$k_b^2 G_{\{xx,yy\}} = \left[ k_b^2 - \partial_{\{x,y\}}^2 \right] (g_- - g_+ - \gamma) + \partial_z^2 (2g_+ + \gamma) \tag{34}$$

$$k_b^2 G_{\{xy,yx\}} = -\partial_x \partial_y (g_- - g_+ - \gamma) \tag{35}$$

$$k_b^2 G_{\{xz,yz\}} = -\partial_{\{x,y\}} \partial_z (g_- + g_+) \tag{36}$$

$$k_b^2 G_{\{zx,zy\}} = -\partial_{\{x,y\}} \partial_z (g_- - g_+) \tag{37}$$

$$k_b^2 G_{zz} = \left[ k_b^2 - \partial_z^2 \right] (g_- - g_+) . \tag{38}$$

In this formulation, direct waves are easily identifiable by their $z - z'$-dependence, that is all terms involving $g_-$. The remaining terms contain $g_+$ and $\gamma$. Because of their $z + z'$-dependence, they must be reflections from the air–Earth interface. As we pointed out above, the direct and reflected waves are treated separately in order to allow the use of 3-D FFTs.

### 4.2.2 *Volume integration of Green's tensor*

For the computation of the elements of the matrix $\mathbf{K}$ (even though $\mathbf{K}^-$ and $\mathbf{K}^+$ are treated separately, this is not explicitly stated here), it is required to compute volume integrals of $\mathbf{G}$ over the discretization blocks. Therefore, many differentiations do not need to be carried out. For the direct component $g_-$ it holds $\frac{\partial g_-}{\partial\{x,y,z\}} = -\frac{\partial g_-}{\partial\{x',y',z'\}}$, while for the reflections from the air–Earth interface $g_+$ and $\gamma$ it holds $\frac{\partial\{g_+,\gamma\}}{\partial\{x,y\}} = -\frac{\partial\{g_+,\gamma\}}{\partial\{x',y'\}}$ and $\frac{\partial\{g_+,\gamma\}}{\partial z} = \frac{\partial\{g_+,\gamma\}}{\partial z}$, respectively. Most of the volume integral terms reduce to more convenient surface and line integrals.

For $R^{\pm} \to 0$, Green's tensor becomes singular. The volume integrals that include the point $R^{\pm} = 0$ are therefore not amenable to numerical integration. In the past, numerous techniques have been proposed as how to deal with this problem. van Bladel (1961) discovered that the integrations exist in a principal value sense, and that the principal value depends on the geometry of the infinitesimal volume. Later on, the more practical expressions to deal with a finite volume have been given by Fikioris (1965). Weidelt (1975) simplified the problem by replacing the concerned block by a sphere of equal volume that also permits analytic integration over the singularity. Gao & Torres-Verdín (2005) demonstrated how the singularity can be avoided by evaluating all integrals over surfaces enclosing the singularity instead of over the volume.

In this paper, we use a technique of singularity removal that has been for example stated by McKirdy (1989). It is intuitively clear that very close to the source, $g_\pm$ may be replaced by the near-field limiting expressions for small $k^2$

$$g_\pm^0 = \frac{1}{4\pi R_\pm}. \tag{39}$$

This can be shown more rigorously by expanding $e^{-kR_\pm}$ around $kR_\pm = 0$. The first term gives then $g_\pm^0$, and all higher order terms are not singular. Furthermore, expression (39) and its derivatives can be integrated analytically. The corresponding antiderivatives are given in Appendix C. Thus, the singular terms can be subtracted, so that the remaining functions can easily be integrated using numerical quadrature. Afterwards, the analytically integrated singular terms are added again.

An additional detail, which to our knowledge has not been mentioned in the literature, is that $\gamma$ contains an additional singularity of the same form as the one in $g_+$. We uncover this by investigating its behaviour for small $k^2$

$$\begin{aligned}\gamma &= \frac{1}{2\pi}\frac{\partial}{\partial z}\left\{\int_0^\infty \frac{1}{\alpha} e^{-\alpha(z+z')} J_0(\kappa r)\mathrm{d}\kappa\right\} \\ &= -\frac{1}{2\pi}\int_0^\infty e^{-\alpha(z+z')} J_0(\kappa r)\mathrm{d}\kappa \\ \gamma^0 &= \lim_{\alpha\to\kappa}\gamma = -\frac{1}{2\pi}\int_0^\infty e^{-\kappa(z+z')} J_0(\kappa r)\mathrm{d}\kappa = -\frac{1}{2\pi R_+} = -2g_+^0\end{aligned} \tag{40}$$

where

$$\alpha^2 = \kappa^2 + k_E^2. \tag{41}$$

Here, we used the Hankel integrals that underlie the solution (38), namely

$$\begin{aligned}\int_0^\infty \frac{\kappa}{\alpha} e^{-\alpha(z+z')} J_0(\kappa r)\mathrm{d}\kappa &= \frac{e^{-k_E R_+}}{R_+} \\ \int_0^\infty \frac{e^{-\alpha(z+z')}}{\alpha} J_0(\kappa r)\mathrm{d}\kappa &= I_0\left[\frac{k_E}{2}\left(R_+ - z - z'\right)\right] \\ &\quad \times K_0\left[\frac{k_E}{2}\left(R_+ + z + z'\right)\right].\end{aligned} \tag{42}$$

The first is the Sommerfeld identity and the second can be found in (Gradshteyn & Ryzhik 2000, eq. 6.637.1).

Because neither of the singularities of $g_+$ or $\gamma$ is located within the domain of integration, both can in principle be ignored. However, close to the Earth surface, the integration converges significantly faster when removing the highly dynamic components $g_+^0$ and $\gamma^0$.

The formulation and integration of magnetic Green's tensor integrals are outlined in Appendix D.

### 4.3 Gradient calculation using the adjoint method

The adjoint method is useful to facilitate the calculation of derivatives in inverse problems by cleverly rearranging the equations, so that often costly, unnecessary computations of intermediate results can be avoided. It is frequently used for the calculation of Fréchet derivatives (e.g. McGillivray & Oldenburg 1990) and the gradients of the objective functional of the inverse problem, but can also be used to calculate columns of the exact Hessian matrix (Fichtner & Trampert 2011).

A very useful review of the adjoint method for gradient computation in general geophysical applications is provided by Plessix (2006). A comprehensive account of the adjoint method in electromagnetics is given by Pankratov & Kuvshinov (2010) and Egbert & Kelbert (2012). Both demonstrate that due to the electromagnetic reciprocity relations, the adjoint problems can be solved using the same system matrix as in the forward problem, even if the particular formulation of the physics is not (complex-)symmetric, as it is the case for the integral equation formulation. This makes it possible to utilize existing forward codes for derivative or gradient calculation. More importantly, if the system matrix has been factorized during the forward solution, the factors can be recycled in the adjoint problem. This can be a great computational advantage. The general adjoint formulation covered by Plessix (2006) does not necessarily yield this result, unless the forward formulation chosen yields a symmetric system matrix. Otherwise, it requires the solution of an adjoint problem different from the forward problem in that it involves the adjoint of the forward system matrix. We choose to use this general formulation, because our implementation relies on an iterative solver, leaving no major advantage of one formulation over the other. In Appendix E, we give a short summary of the adjoint method as well as the resulting expressions for the adjoint problems to be solved for each of the two plane-wave polarizations (eq. E15) and the formula for the gradient (eq. E16). We verified the gradients computed from these expressions against gradients obtained through perturbation of individual model parameters.

### 4.4 Verification of the forward calculation

In order to assess correctness, accuracy and limitations of the forward routine, we conduct a number of synthetic tests. We compare pseudo 2-D responses obtained using a feasible model discretization to those obtained from a well-established 2-D modelling code EMILIA (Siripunvaraporn & Egbert 2000; Kalscheuer *et al.* 2008). We simulate a small, near-surface conductor (50 m × 50 m cross-section) of variable magnitude (10, 100 and 1000 Ωm) in a homogeneous, resistive background (5000 Ωm). Acquisition parameters are similar to the real data case (flight altitude 60 m, field frequency 23.7 kHz, skin depth in the background ≈230 m). Near-surface anomalies require finer discretization than deeply buried bodies, because the plane-wave primary field decays exponentially with depth, and so does its discretization error. We discretize the anomaly with blocks of size 50 m × 50 m × 25 m, which is the discretization we want to use in the inverse problem. The results are shown in Fig. 5, left-hand panel. For 1000 Ωm, the discrepancy is negligible, for 100 Ω-m it is minor and for 10 Ωm, the discrepancy is severe, especially for the real part. Thus, we decide to limit the lowest permissible resistivity in the inversion to 100 Ω-m in order to be able to use this block size. The consequences of this limitation are studied below. In the second experiment (see Fig. 5, right-hand panel), we adapt the discretization to the 10 Ωm–anomaly. The required block size is as small as 10 m × 10 m × 2.5 m, which is currently not feasible on our computers.

## 5 TOPOGRAPHY EFFECTS

Since our forward modelling does not account for the influence of topography on the data, it is worthwhile to assess it. On the one hand, the topography may give rise to induction effects. On the other hand, the air-plane carrying the measurement instruments follows the topography variations, thus inclining the instruments and tilting

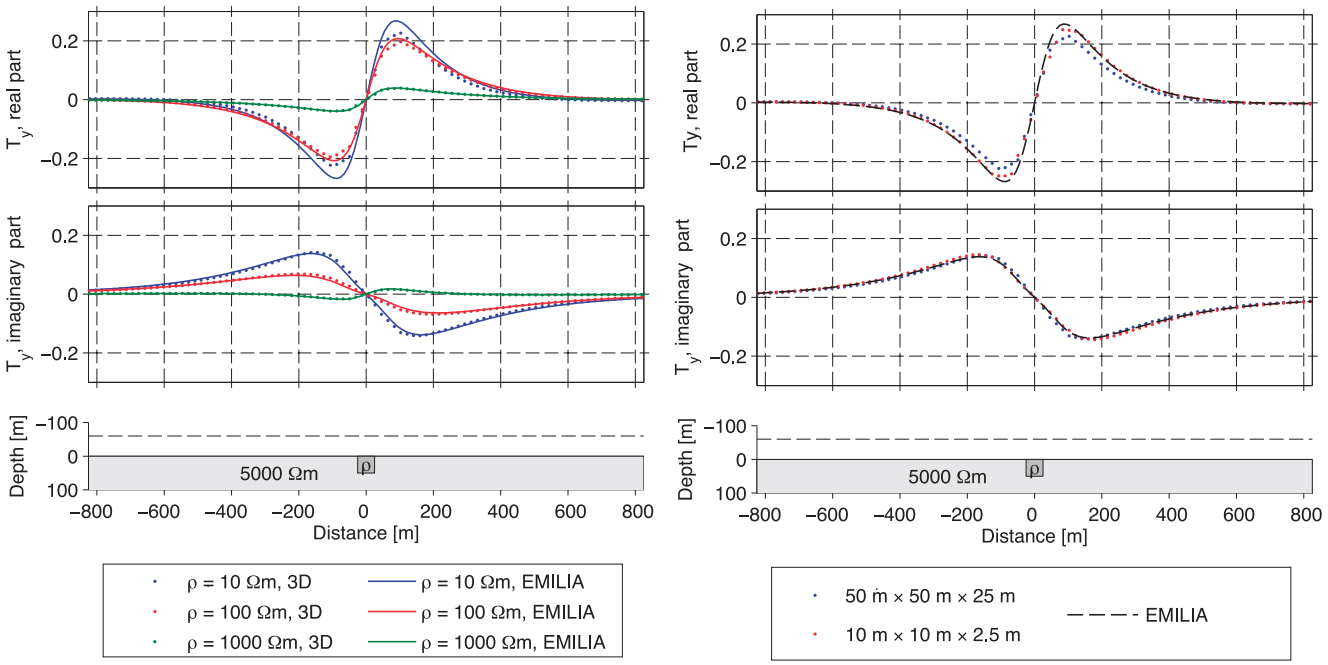


**Figure 5.** Comparison of magnetic transfer functions from the 3-D code and from 2-D modelling code EMILIA. Left-hand panel: variable anomaly magnitude ($\rho$ =10 Ωm, 100 Ωm, 1000 Ωm), fixed discretization (50 m × 50 m × 25 m). Right-hand panel: fixed anomaly magnitude ($\rho$ =10 Ωm), variable discretization (50 m × 50 m × 25 m and 10 m × 10 m × 2.5 m).

the coordinate system against the reference system. The latter effect could theoretically be reversed if the orientation of the air-plane is well known. This is usually not attempted because the tilt of the coordinate system can in fact counteract the distortion due to the topography.

We used 2-D forward modelling to get an image of the extremal cases of topography perpendicular and parallel to the flight direction of the air-plane. In both cases, the transfer functions are propagated to the flight altitude. However, only for a flight direction perpendicular to the valley, the air-plane tilts its nose up or downwards to smoothly follow the topographic variation and maintain its relative altitude. Commonly, this motion is referred to as air-plane pitch. The pitch has to be taken into account when simulating the effect of topography. It can be computed by mathematically rotating the fields in the vertical plane of the flight line prior to transfer function estimation. For a flight direction parallel to the valley, the air-plane remains at a constant height and maintains a horizontal axis. Along a single flight line, there is no variation of the response. Therefore, we model one measurement per flight line parallel to the topography and align them in a profile. Practically, the obtained transfer functions follow from the same computation as the first simulation by omission of the air-plane pitch.

We simulate a valley that deviates from the surrounding flat topography by 60 m. The valley was simulated with and without a conductive sediment fill [see Fig. 6, black lines in panels (a)–(d)] and with a basement of high and intermediate resistivity (5000 Ωm, 1000 Ωm). Finally, we compare the results to a computation that, like our modelling code, neither takes the behaviour of the air-plane nor the topographic variation into account [Fig. 6, red lines in panels (a)–(d)]. Obviously, in the case without conductor, there is no anomaly when the Earth is considered flat.

In order to understand the nature of the topographic distortion, it is useful to first consider flight parallel to topography, that is the pure topographic effect without pitch cancellation [Fig. 6, second row in panels (a)–(d)]. The topography affects mainly the real part of the data. The imaginary part can be considered mostly unaffected. Additionally, the distortion magnitude is larger for a more conductive basement. For a resistive basement, the topography distortion [Fig. 6, panel (a), second row, black lines] and the conductor effect [Fig. 6, panel (b), second row, red lines] are almost in linear superposition [Fig. 6, panel (b), second row, black lines]. For the more conductive basement, the independent effects combine in a more complicated way. The real part is severely distorted.

Next, consider the pitch cancellation effect occurring for flight perpendicular to the topography [Fig. 6, first row in panels (a)–(d)]. The cancellation works better over a more conductive basement, as long as no conductor is involved, because then the topographic influence is more localized than in a resistive basement due to stronger damping. When the conductor is present, at least the peak amplitudes of the anomaly are mostly correct. We can draw the general conclusion that the tipper component along the flight line is much less affected by the topography, meaning that the air-plane inclination generally counteracts at least the low-wavenumber part of the topography effect. For flight lines along the valley, the effect is significant and should be corrected. It should also be noted that topography in general is a 3-D effect on both components of the transfer function. The 2-D cases of topography parallel and perpendicular to the flight direction are external cases that should encompass most non-pathological 3-D situations. Even though it would be best to include the topography into the forward model, this is difficult with our routine, since this would require a very fine vertical discretization.

## 6 SYNTHETIC EXAMPLE

To illustrate the resolution of the VLF method, its limitations and to study the effect of the lower resistivity limit of 100 Ωm, we perform two synthetic tests with pseudo 3-D data computed from a 2-D

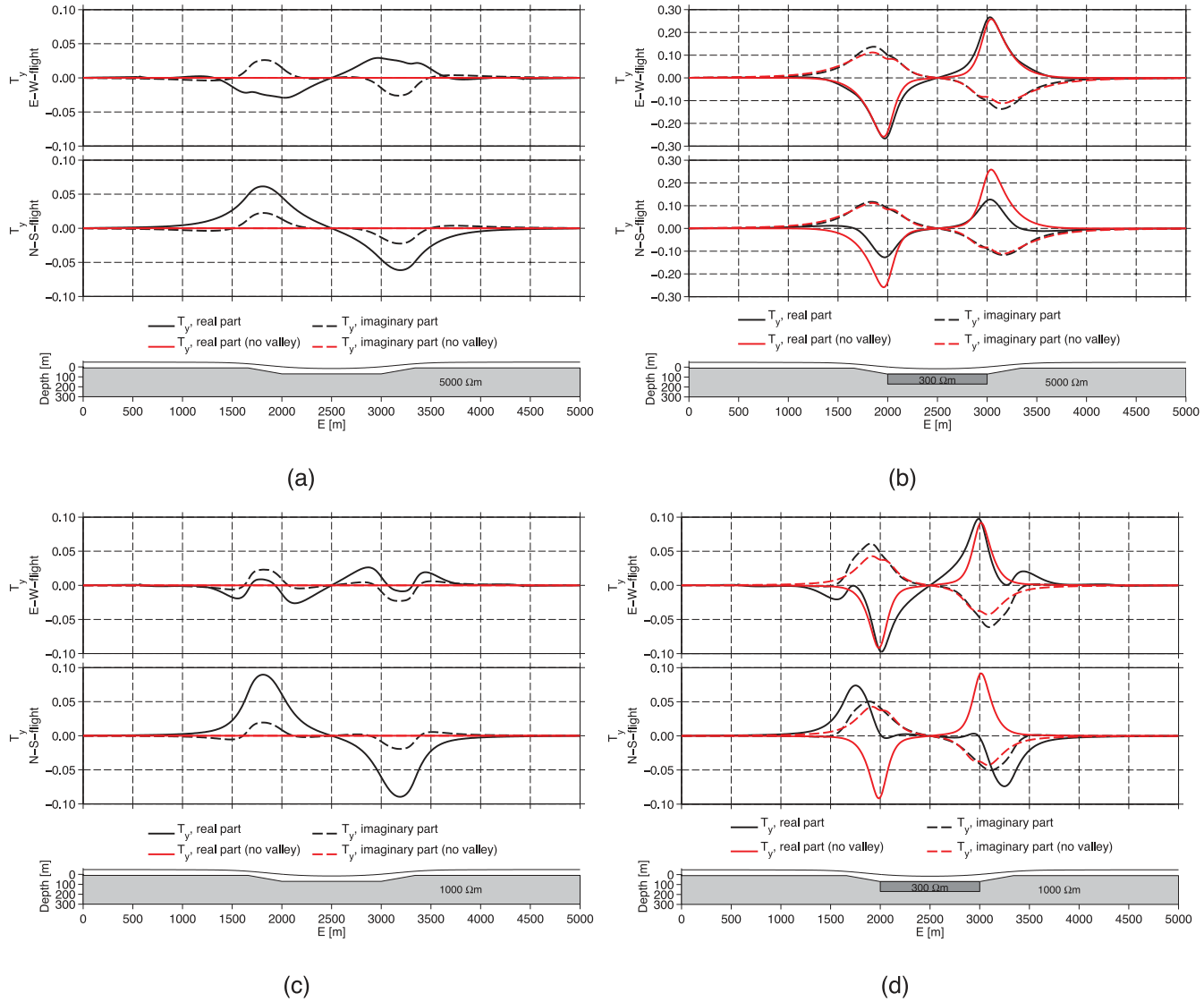


**Figure 6.** Topography effects over a valley of 5000 Ωm(a) and 1000 Ωm(c) and the same with a conductive sediment fill (300 Ωm) added (b), (d). In each panel, the anomaly for flight direction across topography is presented at the top, along the flight direction in the middle, and the resistivity model with a black line marking the flight altitude are displayed at the bottom. The red lines are computations where the topography as well as the flight altitude are considered flat.

model using EMILIA. The data set is simply replicated along strike direction. The synthetic models are depicted in the central row of Fig. 7. In the first experiment, the model contains a shallow conductor of 20 m thickness and a buried, voluminous, eastwards dipping conductor of 10 Ωm in the western half of the model. The same anomalous structures but with 100 Ω-m resistivity are repeated in the eastern half (Fig. 7, left panel). The frequency, flight altitude and background resistivity are identical to those in the previous section. The second experiment is very similar, but the shallow conductor is continued to great depth, while the dipping conductor from first experiment is reduced to its 50 m thick top. The permissible parameter range for the inversion is 100 Ωm $< \rho <$ 10 000 Ωm. Since that data has not been contaminated with synthetic noise, the sole theoretical limit on the data fit is due to the regularization term. Therefore, we arbitrarily stopped the inversion upon reaching a misfit level corresponding to $\sigma_d^2 = (0.015)^2$. We observe that both experiments give practically the same results, illustrating the fact that there is too little energy penetrating through the conductive structures. The conductor top, which is identical in both experiments, is imaged very reliably. This may already be expected from studying the similarity of the anomalies of the two experiments. A further indication gives $z^*$, that is the real part of the *C*-function (Schmucker 1970), which is estimated from the determinant of the impedance tensor (Ward & Hohmann 1988). If interpreted as the *C*-function of a 1-D Earth, it corresponds to the depth to the centre of mass of the in-phase component of the induced currents, similar to the electromagnetic skin-depth in a half-space. It may thus be regarded as a measure for the depth of penetration. Because of the 1-D interpretation required and because there is exactly as much (in-phase) current below $z^*$ as there is above, we believe that this measure is only indicative and possibly conservative. Therefore, we also display $1.5 \times z^*$ as an alternative measure. This is in accordance with the depth of investigation after Spies (1989), even though this author's reasoning is based on a 1-D treatment, which is not possible in the case of magnetic transfer functions. Additionally, the *C*-function contains also the TM-mode (transversal magnetic, i.e. poloidal currents), which

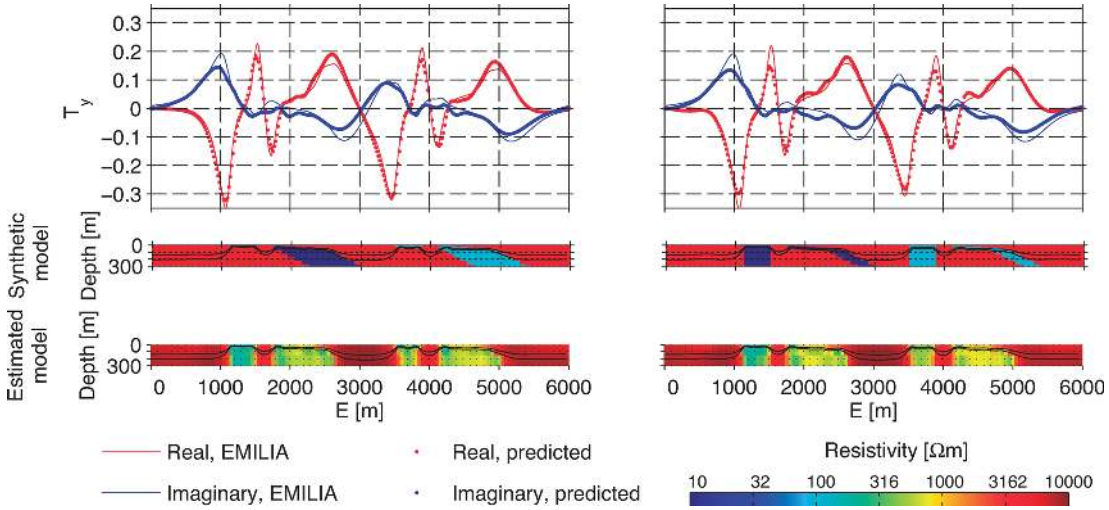


**Figure 7.** Pseudo 3-D data generated by EMILIA, inverted with the 3-D code. Top panel: Simulated (solid line) and predicted (dots) transfer functions. Central row: synthetic models. Bottom panel: pseudo 3-D inversion results. The black line in the models corresponds to 1× and 1.5× the real part of Schmucker's *C*.

does not relate to the purely TE-mode VLF response (transversal electric, i.e. toroidal currents). Our conclusions generally agree well with the detailed resolution analysis provided by Oskooi & Pedersen (2005).

The conductivity of both conductors as well as resistors is generally underestimated. Moreover, due to the conductivity limit in the inversion and the true conductivity anomaly exceeding the limit in the West, the data fit is worse than in the East especially with respect to the peak amplitudes, but we do not observe any structural artefacts.

## 7 FIELD DATA EXAMPLE

### 7.1 Geology

The area of study is located in Lappland (northern Sweden). An overview of the geological situation is presented in Fig. 8. Most rocks in the area are proterozoic and of magmatic origin. Granites are denoted by reddish colours, while the more mafic rocks are depicted in greenish colours. We selected a 10 km×10 km area for inversion.

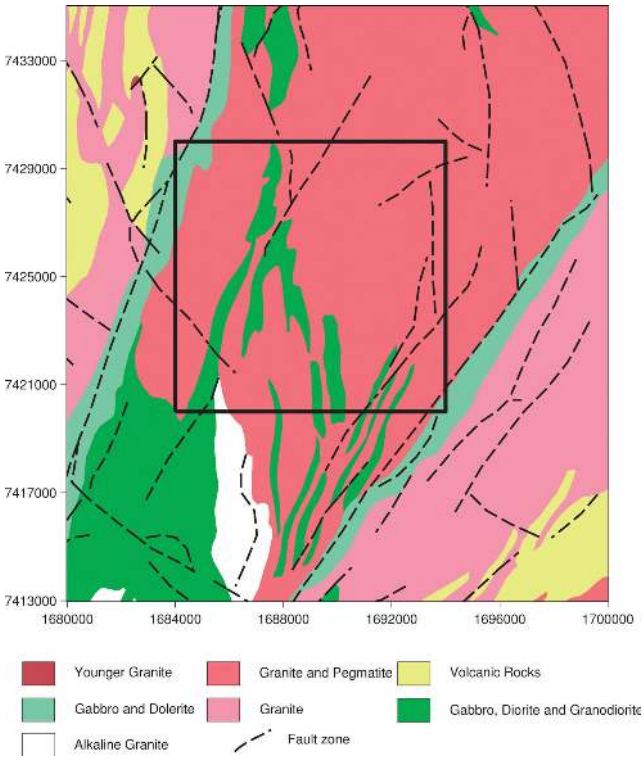


**Figure 8.** Geological map of the study area. The black box indicates the location of the data set used in this example.

### 7.2 Data

The measurements collected are displayed in Fig. 9 (top row). Recordings were taken at 27 103 positions, located along 51 flight lines oriented E–W. The spacing between measurements is circa 20 m, the line spacing is 200 m.

An estimate of the normal-distributed, unbiased part of the measurement noise is available because high wavelengths are strongly damped at flight altitude. Their presence in the recordings is then unquestionably a noise effect. Because the magnetic field in the air is a potential field, the damping can be quantified as $e^{-2\pi h/|\lambda|}$, where $\lambda$ is the wavelength. For small anomalies this is also true for the Tipper, because the anomalous horizontal field is small compared to the normal field and so the Tipper elements can be considered as scaled vertical magnetic fields. Therefore it is possible to choose a threshold, so that all shorter wavelength are classified as noise (for example, 65 dB correspond to $\lambda_{\text{thres}} \approx 50$ m). For Gaussian noise, the spectrum is white. Thus, we can assume equal noise content over all the wavenumber spectrum and derive an estimate of the variance there-from. For the data set shown, we estimate $\sigma^2_{T_x} = (0.029)^2$ and $\sigma^2_{T_y} = (0.017)^2$ ($\sigma^2_{\text{mean}} = (0.024)^2$). This agrees with the visual impression that the $T_x$ component is slightly more noisy.

The estimate is most likely an underestimate because of probable systematic errors in this kind of data. They arise from unprotocolled movements of the aircraft, but also from man-made noise sources. Because this particular area is located in a national park, the influence of man-made infrastructure is assumed negligible. However, the tendency for a very systematic data misfit between the data and the inversion result—or conversely the extremely unrealistic structures required to remove it—indicate that there is still considerable bias in the data. Investigation of other regions from the same data

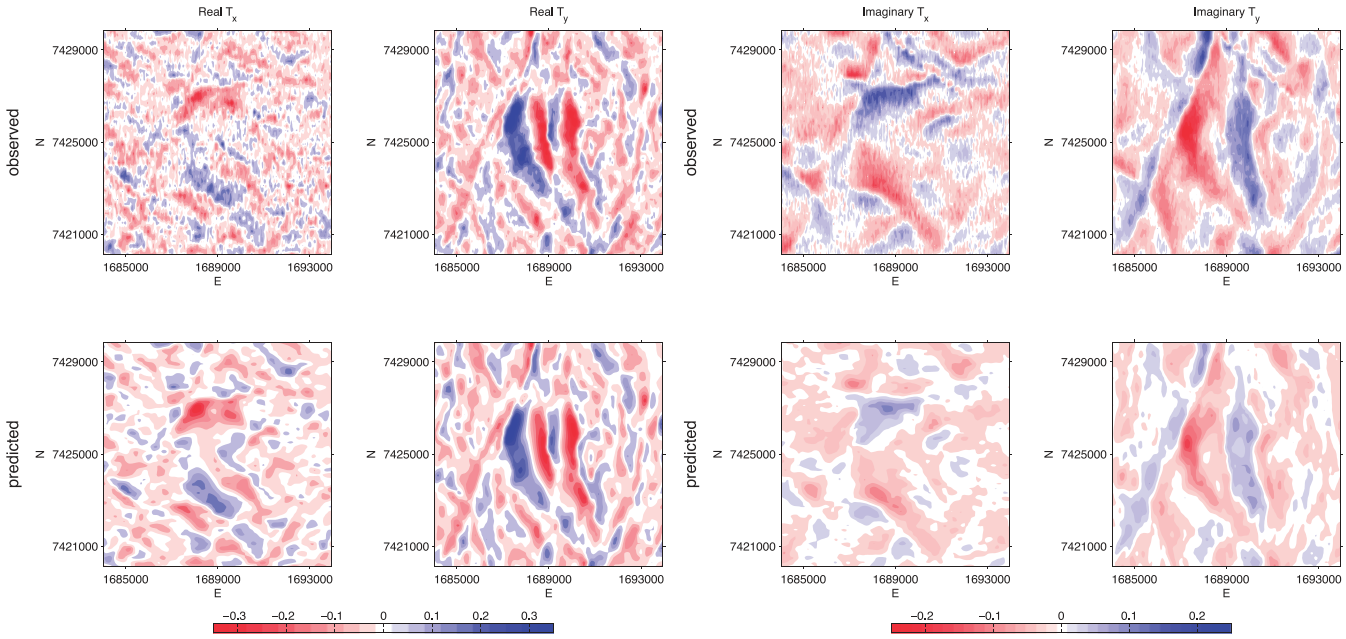


**Figure 9.** Observed VLF anomaly (top panels), compared to predicted anomaly from inversion result (bottom panels). The left-hand panels depict the real part of the data, the imaginary part is displayed on the right. The data is fit to an rms of ≈ 0.034. A conservative estimate of the noise level gives ≈ 0.024.

set lead to the same conclusion. An additional source of apparently biased data misfit is due to disregarding topographic effects.

### 7.3 Inversion

We parametrize the computational domain down to a depth of 600 m. The resistivity of the background half-space is chosen as 5000 Ωm. The forward model is uniformly discretized using a block size of 50 m × 50 m × 25 m, whereas the layer thickness of the model for the inversion increases with depth. The first layer is 25 m thick and each following layer is twice as thick as the previous one. The model grid is laterally extended by 750 m (>3 times the skin depth in the background) around the data covered region, in order to avoid truncation effects. This margin is removed from the model after the inversion. The forward problem consists of 227 × 230 × 24 × 3 field quantities (≈3.8 × $10^6$ unknowns). We invert for 227 × 230 × 5 model blocks (≈2.6 × $10^5$ unknowns). The inversion stopped at iteration number 10 and took in total two hours on 12 CPUs.

### 7.4 Inversion result

The inversion result explains all data to an rms of ≈0.034. The estimated data is displayed in Fig. 9 (bottom row). While the overall picture is in consistent with the observations, there is a systematic underestimation of the imaginary parts throughout. For the reasons given above, we believe that the data is biased.

The upper 150 m of the inversion result are shown in Fig. 10. The lower layers mostly exceed the $z^*$ measure for penetration depth considerably. Only the most resistive structures can be resolved at even greater depth. An impression of this is given in slices through the 3-D model in Fig. 11, where $z^*$ and $1.5\times z^*$ are included.

Fig. 10 also shows on the right-hand panel an apparent resistivity map derived from the data (Becken & Pedersen 2003). The long wavelength features are in excellent agreement with the inversion model, but conductivity amplitudes are much less dynamic. This can be expected because the transformation implies a half-space assumption and consequently involves averaging to a certain degree. For the same reasons, the inversion is able to reproduce features of much larger wavenumber and therefore a more detailed image in the lateral directions, as the one available from the map interpretation. It has been demonstrated in the synthetic studies above (Section 6), that we can only expect vertical resolution to a certain extent, namely down to where the first conductor is encountered. This manifests itself in predominantly vertical contrasts as shown in Fig. 11. Resistive structures underneath the conductive top may be shielded. A dipping conductive top can, however, be reliably resolved. As an example, both slices show at ≈1 690 000E a westward dipping conductor, a feature that can not be suspected to exist from the apparent resistivity map alone.

Fig. 12 shows a conductor–resistor map. Therein, the inclination of this conductor can be followed for several kilometres from ≈7 423 000N to ≈7 427 000N. The map demonstrates that especially faults or weakness zones at geological contacts are often associated with lower resistivity (Fig. 12, left-hand panel). We believe that fractures give passage to water that permits current flow. Highly resistive zones often coincide with topographic highs (Fig. 12, right-hand panel). One possible explanation is that since the topography in the area is mostly formed by the movement of glaciers during the last glacial, hills and mountains may be related to structurally stable regions that withstood the erosional forces. They may thus lack fracture zones and other fluid passage ways. Another possible reason for the correlation is that topographic lows are associated with extended wetlands that yield an elevated conductivity at the surface, masking possible buried resistors.

## 8 CONCLUSIONS

We have developed a large-scale inversion method for airborne tensor VLF data in order to increase the utility of the Swedish VLF data set beyond map-based interpretation. This is the first time it that a 3-D inversion of this kind of data has been attempted. Because of the discrepancy between the model scale of interest (kilometres)

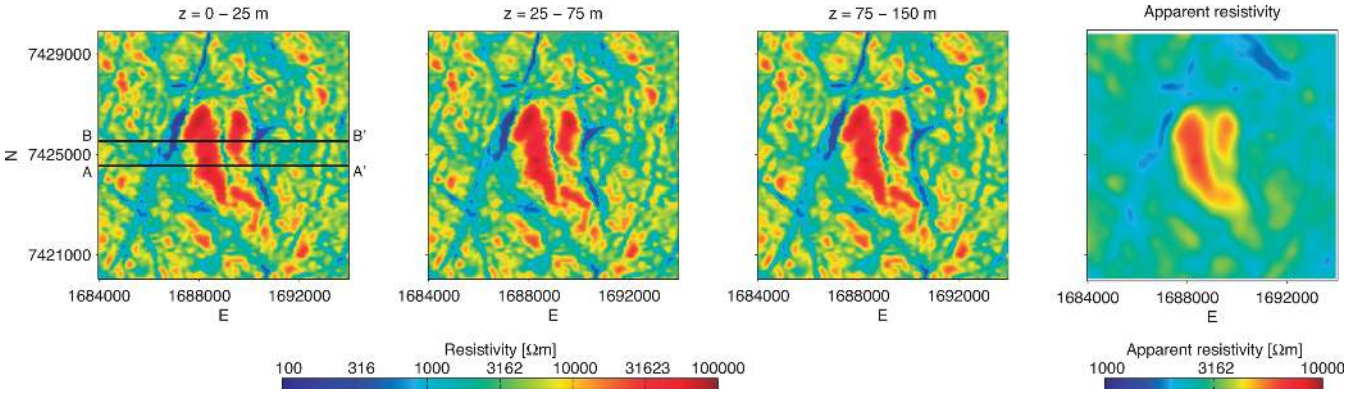


**Figure 10.** The uppermost three layers of the inversion result (first three panels) in comparison to the apparent resistivity map derived from the data using the transformation introduced by Becken & Pedersen (2003). Deeper layers are not shown because they are mostly unresolved. Two selected sections, denoted as A–A′ and B–B′ in the leftmost panel, are shown in Fig. 11.

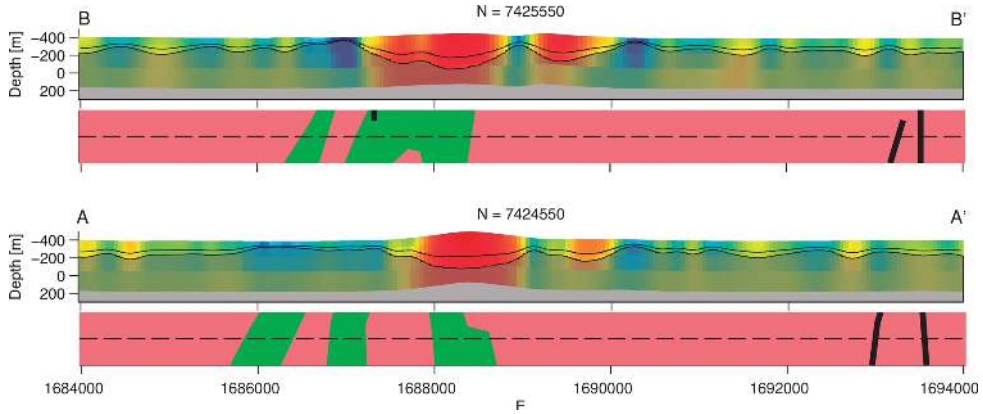


**Figure 11.** E–W slices (B–B′ and A–A′, compare Fig. 10) through the resistivity model at two different latitudes. Same colour scale as in Fig. 10. Beneath each slice, the corresponding part of the surface geological map is shown for comparison (see legend on Fig. 8), on which the dashed line marks the outcrop of the section. The shallow black line indicates $z^*$, a conservative measure of penetration depth (see text). The deeper black line is $z^*$ multiplied by 1.5. The area below is shaded since it marks the less well-constrained structures and care must be taken in the interpretation.

and the wavelength of the relatively high-frequency fields (tens of metres), the implementation of a computationally feasible forward modelling was challenging. The fundamental aspects are the exploitation of certain symmetry properties of Green's tensor, so that 3-D FFTs are applicable in the evaluation of matrix products required by the iterative system solver, and a novel nested grid approximation that effectively limits the computational effort on each grid scale to the respective important wavelength. It is noteworthy that even though the latter approximation introduces a significant error to the fields modelled within the Earth, the responses in the air are practically unaffected. We conclude that the errors are well behaved in the sense that they cancel during averaging. An additional concern is that the discretization requirements increase with conductivity. Since the block size is prescribed, it is necessary to limit the lowest resistivity in the inversion. Most of Sweden is located on a highly resistive crystalline bedrock. Therefore, the bulk of the data set can be treated with the method as described, but an adaptation of the discretization is undoubtedly necessary for data collected over the sea or over mineral bearing districts such as the mining areas in the country. The choice of NLCG as an inversion algorithm is motivated by the low memory requirements.

Since the modelling at present does not respect topography, we evaluated its influence in synthetic studies and found that it can considerably bias the responses, especially for topography variations perpendicular to the flight direction. Variations along the flight direction are counteracted to a certain extent by the air-plane, which by smoothly following the landscape causes a contrarious effect. For a modelling of these effects, it would also be necessary to record the air-plane orientation precisely.

In the application of the inversion to synthetic and field examples we can pinpoint the improvements of an inversion against a map-based interpretation. While the vertical variations resolved are as expected limited, the top of conductive structures is a well-defined feature. For example, dip directions of dipping conductors can be estimated. Additionally, the inversion results have a very high lateral resolution due to the data density, so that contrasts, especially at the surface, are very pronounced. This focussing is a property of the inversion, because a part of it is the inversion of the smoothing that the anomalous electromagnetic fields undergo during the propagation from the causative structures to the measurement level in the air. Furthermore, the inversion result represents a model of reality that is physically consistent with the data. This can never be a property of map representations.

In particular, a very good correlation is found between elongated conductor systems and known geological features, such as geological contacts and associated fracture zones, as well as faults. The conductors suggest in many cases the presence of structures that are not found in the geological map, or only partially. Resistors correlate well with topographic highs, which is due to the lack of wet sediments on the crystalline ridges and because those are

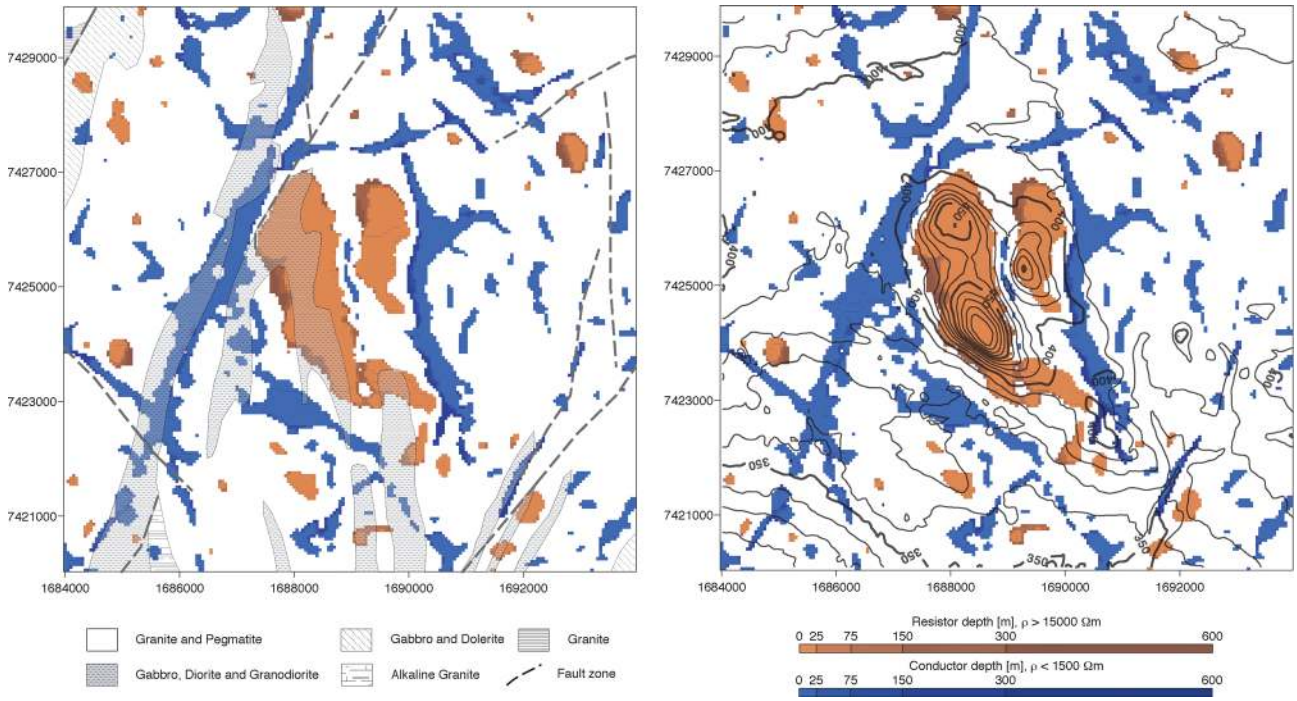


**Figure 12.** Comparison of conductors ($\rho < 1500$ Ωm, blue) and resistors ($\rho > 15000$ Ωm, red) with the surface geology (left-hand panel) and the topography (right-hand panel). Bright colours indicate shallow, dark colours deep structures.

possibly very intact, which is indicated by their remaining after heavy glacial erosion. Buried resistors in the lower areas are not easily resolved, since there are usually extended swamps and thus, surface conductivity is elevated and masks the resistive rocks to a certain extent.

## ACKNOWLEDGEMENTS

The authors wish to express their gratitude to the Swedish Geological Survey for giving permission to use the VLF data set presented here.

## REFERENCES

Alumbaugh, D. & Newman, G., 1997. Three-dimensional massively parallel electromagnetic inversion. 2. Analysis of a crosswell electromagnetic experiment, *Geophys. J. Int.,* **128**(2), 355–363.

Aster, R.C., Borchers, B. & Thurber, C.H., 2005. *Parameter Estimation and Inverse Problems,* Academic Press.

Avdeev, D. & Avdeeva, A., 2009. 3D magnetotelluric inversion using a limited-memory quasi-newton optimization, *Geophysics,* **74**(3), F45–F57.

Avdeev Dmitry, B., Kuvshinov, A.V., Pankratov, O.V. & Newman, G.A., 1997. High-performance three-dimensonal electromagnetic modelling using modified Neumann series. Wide-band numerical solution and examples, *J. Geomagn. Geoelec.,* **49,** 1519–1539.

Becken, M. & Pedersen, L.B., 2003. Transformation of vlf anomaly maps into apparent resistivity and phase, *Geophysics,* **68**(2), 497–505.

Bhattacharyya, B.K., 1964. Magnetic anomalies due to prism-shaped bodies with arbitrary polarization, *Geophysics,* **29**(4), 517–531.

Blakely, R.J., 1995. *Potential Theory in Gravity & Magnetic Applications,* Cambridge Univ. Press.

Christensen, N.B., 1990. Optimized fast Hankel transform filters, *Geophys. Prospect.,* **38**(5), 545–568.

Constable, S.C., Parker, R.L. & Constable, C.G., 1987. Occam's inversion: a practical algorithm for generating smooth models from electromagnetic sounding data, *Geophysics,* **52**(3), 289–300.

Cooley, J.W. & Tukey, J.W., 1965. An algorithm for machine calculation of complex Fourier series, *Math. Comput.,* **19**(90), 297–301.

Cox, L.H., Wilson, G.A. & Zhdanov, M.S., 2010. 3D inversion of airborne electromagnetic data using a moving footprint, *Explor. Geophys.,* **41**(4), 250–259.

Egbert, G.D. & Kelbert, A., 2012. Computational recipes for electromagnic inverse problems, *Geophys. J. Int.,* **189,** 251–267.

Fichtner, A. & Trampert, J., 2011. Hessian kernels of seismic data functionals based upon adjoint techniques, *Geophys. J. Int.,* **185,** 775–798.

Fikioris, J.G., 1965. Electromagnetic field inside a current-carrying region, *J. Math. Phys.,* **6**(11), 1617–1620.

Gao, G. & Torres-Verdín, 2005. Analytical techniques to evaluate the integrals of 3D and 2D spatial dyadic Green's functions, *Prog. Electromagn. Res,* **52,** 47–80.

Gradshteyn, I.S. & Ryzhik, I.M., 2000. *Table of Integrals, Series, and Products,* 6th edn, Academic Press, translated from the Russian.

Grayver, A.V., Streich, R. & Ritter, O., 2013. Three-dimensional parallel distributed inversion of CSEM data using a direct forward solver, *Geophys. J. Int.,* **193**(3), 1432–1446.

Hohmann, G.W., 1975. Three-dimensional induced polarization and electromagnetic modeling, *Geophysics,* **40**(2), 309–324.

Holtham, E. & Oldenburg, D.W., 2010. Three-dimensional inversion of ZTEM data, *Geophys. J. Int.,* **182,** 168–182.

Holtham, E. & Oldenburg, D.W., 2012. Large-scale inversion of ZTEM data, *Geophysics,* **77**(4), WB37–WB45.

Hursan, G. & Zhdanov, M.S., 2002. Contraction integral equation method in three-dimensional electromagnetic modeling, *Radio Sci.,* **37**(6).

Kaikkonen, P., Sharma, S.P. & Mittal, S., 2012. 3D modeling and inversion of VLF and VLF-R electromagnetic data, *Geophysics,* **77**(4), WB219–WB231.

Kalscheuer, T., Pedersen, L.B. & Siripunvaraporn, W., 2008. Radiomagnetotelluric two-dimensional forward and inverse modelling accounting for displacement currents, *Geophys. J. Int.,* **175**(2), 486–514.

Mackie, R.L. & Madden, T.R., 1993. 3-Dimensional magnetotelluric inversion using conjugate gradients, *Geophys. J. Int.,* **115**(1), 215–229.

McGillivray, P.R. & Oldenburg, D.W., 1990. Methods for calculating Fréchet derivatives and sensitivities for the non-linear inverse problem: a comparative study, *Geophys. Prospect.,* **38,** 499–524.

McKirdy, D.M., 1989. Recent improvements to the application of the volume integral method of eddy current modeling, *J. Nondestr. Eval.,* **8**(1), 45–52.
Millard, X. & Liu, Q.H., 2003. A fast volume integral equation solver for electromagnetic scattering from large inhomogeneous objects in planarly layered media, *IEEE Trans. Antennas Propag.,* **51**(9), 2393–2401.
Newman, G.A. & Alumbaugh, D.L., 1997. Three-dimensional massively parallel electromagnetic inversion—I. theory, *Geophys. J. Int.,* **128**(2), 345–354.
Newman, G.A. & Alumbaugh, D.L., 2000. Three-dimensional magnetotelluric inversion using non-linear conjugate gradients, *Geophys. J. Int.,* **140,** 410–424.
Nie, X., Li, L.-W., Yuan, N. & Yeo, T.S., 2013. A fast integral equation solver for 3D induction well logging in formations with large conductivity contrasts, *Geophys. Prospect.,* **61,** 645–657.
Nocedal, J. & Wright, S.J., 2006. *Numerical Optimization,* 2nd edn, Springer.
Oskooi, B. & Pedersen, L.B., 2005. Resolution of airborne VLF data, *J. Appl. Geophys.,* **58,** 158–175.
Pankratov, O. & Kuvshinov, A., 2010. General formalism for the efficient calculation of derivatives of EM frequency domain responses and derivatives of the misfit, *Geophys. J. Int.,* **181,** 229–249.
Pedersen, L.B., Qian, W., Dynesius, L. & Zhang, P., 1994. An airborne tensor VLF system. from concept to realization, *Geophys. Prospect.,* **42,** 863–883.
Pedersen, L.B., Persson, L., Bastani, M. & Byström, S., 2009. Airborne VLF measurements and mapping of ground conductivity in Sweden, *J. appl. Geophys.,* **67,** 250–258.
Phillips, J.R. & White, J.K., 1996. A precorrected-FFT method for electrostatic analysis of complicated 3-D structures, *IEEE Trans. Comput. Aided Des. Integr. Circuits Syst.,* **16**(10), 1059–1071.
Plessix, R.-E., 2006. A review of the adjoint-state method for computing the gradient of a functional with geophysical applications, *Geophys. J. Int.,* **167,** 495–503.
Polak, E. & Ribière, G., 1969. Note sur la convergence de methodes de directions conjuguèes, *Revue française d'informatique et de recherche opérationnelle,* **16,** 35–43.
Raiche, A.P., 1974. An integral equation approach to three-dimensional modelling, *Geophys. J. R. astr. Soc.,* **36,** 363–376.
Raiche, A.P., 1975. Analytical Green's tensors for integral-equation modeling, *Geophys. J. R. astr. Soc.,* **42**(3), 1035–1038.
Remmert, R., 1991. *Theory of Complex Functions,* Springer.
Rodi, W. & Mackie, R.L., 2001. Nonlinear conjugate gradients algorithm for 2-D magnetotelluric inversion, *Geophysics,* **66**(1), 174–187.
Sasaki, Y., 2001. Full 3-D inversion of electromagnetic data on PC, *J. appl. Geophys.,* **46**(1), 45–54.
Schmucker, U., 1970. An introduction to induction anomalies, *J. Geomagn. Geoelec.,* **22**(1–2), 9–33.
Siripunvaraporn, W. & Egbert, G., 2000. An efficient data-subspace inversion method for 2-D magnetotelluric data, *Geophysics,* **65**(3), 791–803.
Siripunvaraporn, W. & Egbert, G., 2009. WSINV3DMT: vertical magnetic field transfer function inversion and parallel implementation, *Phys. Earth planet. Inter.,* **173,** 317–329.
Siripunvaraporn, W., Egbert, G., Lenbury, Y. & Uyeshima, M., 2005. Three-dimensional magnetotelluric inversion: data-space method, *Phys. Earth planet. Inter.,* **150,** 3–13.
Spies, B.R., 1989. Depth of investigation in electromagnetic sounding methods, *Geophysics,* **54**(7), 872–888.
Tseng, H.-W., Lee, K.H. & Becker, A., 2003. 3D interpretation of electromagnetic data using a modified Born approximation, *Geophysics,* **68**(1), 127–137.
van Bladel, J., 1961. Some remarks on Green's dyadic for infinite space, *IRE Trans. Anntenas Propag.,* **AP-9,** 563–566.
Vijayakumar, S. & Cormack, D.E., 1988. An invariant embedding method for singular integral evaluation on finite domains, *SIAM J. Appl. Math.,* **48**(6), 1335–1349.
Vozoff, K., 1972. Magnetotelluric method in exploration of sedimentary basins, *Geophysics,* **37**(1), 98–171.
Wannamaker, P.E., Hohmann, G.W. & SanFilipo, W.A., 1984. Electromagnetic modeling of three-dimensional bodies in layered Earths using integral equations, *Geophysics,* **49**(1), 60–74.
Ward, S.H. & Hohmann, G.W., 1988. Electromagnetic theory for geophysical applications, in *Electromagnetic Methods in Applied Geophysics,* Vol. 1: Theory, pp. 131–311, ed. Nabighian, M. N., Society of Exploration Geophysicists.
Weidelt, P., 1975. Electromagnetic induction in three-dimensional structures, *J. Geophys.,* **41,** 85–109.
Zhdanov, M.S., 2002. *Geophysical Inverse and Regularization Problems,* 1st edn, Elsevier Science B. V.
Zhdanov, M.S., Green, A., Gribenko, A. & Cuma, M., 2010. Large-scale three-dimensional inversion of EarthScope MT data using the integral equation method, *Izv. Phys. Solid Earth,* **46**(8), 670–678.

## APPENDIX A: DISCRETIZATION OF THE INTEGRAL EQUATION

The integral equation (10) can be rearranged in the following way

$$\sum_{j=x,y,z}\int_{V'}\left\{\left[\delta_{ij}\delta(\mathbf{r}-\mathbf{r}')+\left(\mathbf{G}_j(\mathbf{r}'|\mathbf{r})\cdot\hat{\mathbf{u}}_i\right)k_a^2(\mathbf{r}')\right]\hat{\mathbf{u}}_j\right\}\cdot\mathbf{E}(\mathbf{r}')\mathrm{d}V'$$
$$=\mathbf{E}_p(\mathbf{r})\cdot\hat{\mathbf{u}}_i. \tag{A1}$$

Here, we used the identity

$$\mathbf{E}(\mathbf{r})\cdot\hat{\mathbf{u}}_i=\sum_{j=x,y,z}\delta_{ij}\int_{V'}\delta(\mathbf{r}-\mathbf{r}')\mathbf{E}(\mathbf{r}')\cdot\hat{\mathbf{u}}_j\mathrm{d}V' \tag{A2}$$

with the Kronecker symbol

$$\delta_{ij}=\begin{cases}1 & i=j\\ 0 & i\neq j\end{cases}. \tag{A3}$$

In order to discretize eq. (A1) we make the same approximations as Weidelt (1975) or Hohmann (1975):

(i) The computational domain is bounded, that is no anomalies are found outside of it or they are sufficiently far away to be ignored.
(ii) The domain is subdivided into block-shaped volumes (cells) within each of which the anomalous conductivity $\sigma_a$ and the electric field $\mathbf{E}$ are approximated by constant functions (pulse basis functions).
(iii) For the constant value of the fields, we use the value at the midpoint of each block.

Because of the approximations (ii) and (iii), a common index $k$ can be assigned to the respective block volume $V_k$ and the same block's midpoint position $\mathbf{r}_k$. The discretized electric field $\mathbf{E}$ consists then of discrete values

$$E_m=E_{\tau_1(i,k)}=E_i(\mathbf{r}_k)=\mathbf{E}(\mathbf{r}_k)\cdot\hat{\mathbf{u}}_i, \tag{A4}$$

where

$$m=\tau_1(i,k) \tag{A5}$$

is some bijective mapping from the spatial index set $k$ and the indices $i$ denoting the components of the 3-D field vector $\mathbf{E}(\mathbf{r}_k)$ to a set of collective indices $m$.

Approximation (ii) may be expressed as

$$\int_{V_l}\delta_{ij}\delta(\mathbf{r}-\mathbf{r}')E_j(\mathbf{r}')\mathrm{d}V'\approx E_{\tau_1(j,l)}\cdot\int_{V_l}\delta_{ij}\delta(\mathbf{r}-\mathbf{r}')\mathrm{d}V'$$
$$\int_{V_l}G_{ji}(\mathbf{r}'|\mathbf{r})k_a^2(\mathbf{r}')E_j(\mathbf{r}')\mathrm{d}V'\approx k_{a,l}^2E_{\tau_1(j,l)}\cdot\int_{V_l}G_{ji}(\mathbf{r}'|\mathbf{r})\mathrm{d}V'. \tag{A6}$$

Using this, we can now write a discretized version of eq. (A1), namely

$$\sum_{j=x,y,z}\sum_{l}\left[\int_{V_l}\delta_{ij}\delta(\mathbf{r}_k-\mathbf{r}')\mathrm{d}V'\right.$$

$$\left.+\int_{V_l}G_{ji}(\mathbf{r}'|\mathbf{r}_k)\mathrm{d}V'\cdot k_{a,l}^2\right]\cdot E_{\tau_1(j,l)}=E_{p,\tau_1(i,k)}. \quad (A7)$$

The remaining definite integrals depend only on the background conductivity and the discretization, and can thus be evaluated and tabulated in advance. The former set of integrals on the left-hand side can be identified with the components of a unit matrix $\mathbf{I}$ with dimensions corresponding to field discretization

$$I_{mn}=\int_{V_l}\delta_{ij}\delta(\mathbf{r}_k-\mathbf{r}')\mathrm{d}V'=\delta_{ij}\delta_{kl}=\delta_{\tau_1(i,k),\tau_1(j,l)}=\delta_{mn} \quad (A8)$$

where $n=\tau_1(j,\,l)$. The latter integrals contain the elements of Green's tensor. They are organized in the electric kernel matrix $\mathbf{K}$ in the following way:

$$K_{mn}=K_{\tau_1(i,k),\tau_1(j,l)}=\int_{V_l}G_{ij}(\mathbf{r}_k|\mathbf{r}')\mathrm{d}V'. \quad (A9)$$

Note that by electromagnetic reciprocity, cause and effect of an electromagnetic field may be interchanged:

$$\int_{V_l}G_{ji}(\mathbf{r}'|\mathbf{r}_k)\mathrm{d}V'=\int_{V_l}G_{ij}(\mathbf{r}_k|\mathbf{r}')\mathrm{d}V'. \quad (A10)$$

Next, the anomalous conductivity values of the blocks are sorted into the diagonal matrix $\Sigma$, which then has the entries

$$\Sigma_{mn}=\Sigma_{\tau_1(i,k),\tau_1(j,l)}=\delta_{ij}\delta_{kl}k_{a,k}^2. \quad (A11)$$

With

$$\mathbf{A}=\mathbf{I}+\mathbf{K}\Sigma \quad (A12)$$

eq. (A7) can be written as

$$\mathbf{AE}=\mathbf{E}_p \quad (A13)$$

as a discrete approximation to eq. (10).

The elements of the magnetic kernel matrix in the discrete approximation (19) to eq. (15) are

$$K_{M,mn}=K_{M,\tau_1(i,\tilde{k}),\tau_1(j,l)}=\int_{V_l}M_{ij}(\mathbf{r}_{\tilde{k}}|\mathbf{r}')\mathrm{d}V', \quad (A14)$$

where the measurement positions are denoted as $\mathbf{r}_{\tilde{k}}$, which are spatially ordered by an index set $\tilde{k}$ different from the set $k$.

## APPENDIX B: MATRIX MULTIPLICATIONS USING 3-D FFTs

Here, we describe the evaluation of the matrix vector products involving the kernel matrix $\mathbf{K}$ in detail.

It is convenient for the following explanation to express the spatial index set $k$ by its 1-D constituent indices $k_x$, $k_y$, $k_z$, which label the blocks and their midpoints along the Cartesian axes. Another bijective mapping

$$k=\tau_2(k_x,k_y,k_z) \quad (B1)$$

similar to $\tau_1$ (expression A5) relates them to $k$. For an anomalous domain consisting of $N_x\times N_y\times N_z$ blocks, we have

$$k_{\{x,y,z\}}=1,2,\ldots,N_{\{x,y,z\}}. \quad (B2)$$

The field and current vectors that $\mathbf{K}$ or $\mathbf{K}^\dagger$ have to be multiplied with are then arranged as, for example,

$$E_{\tau_1[i,\tau_2(k_x,k_y,k_z)]}=\mathbf{E}(x_{k_x},y_{k_y},z_{k_z})\cdot\hat{\mathbf{u}}_i:=E_{i,(k_x,k_y,k_z)}. \quad (B3)$$

Next, we introduce a corresponding notation for the elements of $\mathbf{K}$, namely

$$K_{mn}=K_{\tau_1[i,\tau_2(k_x,k_y,k_z)],\tau_1[j,\tau_2(l_x,l_y,l_z)]}$$

$$=\int_{V_l}G_{ij}(x_{k_x},y_{k_y},z_{k_z}|x',y',z')\mathrm{d}V':=K_{ij,(k_x,k_y,k_z|l_x,l_y,l_z)}. \quad (B4)$$

First, $\mathbf{K}$ is separated according to eq. (25). Then, each part of $\mathbf{K}^-$ corresponding to one tensor component has a nested block Toeplitz structure, that is it is a block Toeplitz matrix where the blocks are recursively either block Toeplitz or Toeplitz matrices (matrices where blocks/elements are repeated along the diagonals). The structure of the corresponding parts of $\mathbf{K}^+$ can be called nested block Toeplitz-Hankel (Hankel matrices are upside down Toeplitz matrices), because the field indices $l_z$ of the column dimension appear in reversed order ($\tilde{l}_z=N_z+1-l_z$). As a consequence, each of the matrices is, up to the complications at the domain boundary, fully defined by three matrix rows (one for $i=x,\,y,\,z$). The elements to be tabulated are

$$K^-_{ij,(0,0,0|k_x,k_y,k_z)}$$

$$k_{\{x,y,z\}}=-N_{\{x,y,z\}}+1,\ldots,N_{\{x,y,z\}}-1 \quad (B5)$$

and

$$K^+_{ij,(0,0,0|k_x,k_y,k_z)}$$

$$k_{\{x,y\}}=-N_{\{x,y\}}+1,\ldots,N_{\{x,y\}}-1$$

$$k_z=1,\ldots,2N_z-1, \quad (B6)$$

respectively, abbreviated as $\mathcal{K}^{\pm}_{ij}$ in a more condensed notation. The source is located in the midpoint of block $k_x=k_y=k_z=0$. The index range is constrained to be large enough so that the source block and field point can lie on opposite ends of the anomalous domain. The product of $\mathbf{K}^-$ and a vector $\mathbf{f}$ reads

$$\sum_n K^-_{mn}f_n=\sum_j\sum_{l_x,l_y,l_z}K^-_{ij,(k_x,k_y,k_z|l_x,l_y,l_z)}f_{j,(l_x,l_y,l_z)}$$

$$=\sum_j\sum_{l_x,l_y,l_z}K^-_{ij,(0,0,0|l_x-k_x,l_y-k_y,l_z-k_z)}f_{j,(l_x,l_y,l_z)}. \quad (B7)$$

This can be expressed using the 3-D convolution operator $***$, that is

$$\mathbf{K}^-\mathbf{f}=\sum_j\left(\updownarrow_{x,y,z}\mathcal{K}^-_{ij}\right)***f_j. \quad (B8)$$

The symbol $\updownarrow$ marks the reversal of the indices along the subscripted dimensions. Similarly, $\mathbf{K}^+\mathbf{f}$ can be written as

$$\mathbf{K}^+\mathbf{f}=\updownarrow_z\left[\sum_j\left(\updownarrow_{x,y,z}\mathcal{K}^+_{ij}\right)***f_j\right]. \quad (B9)$$

The adjoint operations are given by

$$(\mathbf{K}^{-})^{\dagger}\mathbf{f} = \sum_i \overline{\mathcal{K}}_{ij}^{-} * * * f_i \tag{B10}$$

$$(\mathbf{K}^{+})^{\dagger}\mathbf{f} = \sum_i \overline{\mathcal{K}}_{ij}^{+} * * * \left(\updownarrow_z f_i\right). \tag{B11}$$

The reversal along the vertical direction in the products involving $\mathbf{K}^{+}$ reflects the reversal of the matrix structure from Toeplitz to Hankel. The result of eq. (B9) as well as the argument to (B11) is subject to this reversal. In the adjoint product relations (B10) and (B11), the matrix adjunction manifests itself in the role inversion of the summation indices, the complex conjugation and that all three space dimensions of the kernel are reversed when compared to the eqs (B8) and (B9).

As indicated earlier, the convolutions can be calculated as the inverse Fourier transform of the product of the wavenumber spectra of $\mathbf{K}^{\pm}$ and $\mathbf{f}$, using FFT algorithms. Since neither Green's tensor nor any of the field quantities are periodic, the convolution is non-circular. A non-circular discrete convolution of finite signals can then be equivalently performed in discrete Fourier domain, if the spectra of the input signals are sufficiently well sampled, so that their product includes all wavenumber components required to represent the complete spectrum of the convolution. For two signals of length $N_1$ and $N_2$, their convolution has $N_1 + N_2 - 1$ non-zero elements. This means, that $\mathbf{K}^{\pm}$ and $\mathbf{f}$ both require adequate extension with zeros prior to taking the Fourier transform. Likewise, components of the resulting inverse Fourier transforms that lie outside of the spatial domain of $\mathbf{f}$ are discarded.

Also note that the spectrum of the kernel only needs to be computed once as a part of the kernel preparation. During the iterations, the matrix vector product can be carried out using one additional FFT and one inverse FFT for every one of the nine combinations of $i$ and $j$.

## APPENDIX C: ANALYTICAL INTEGRALS FOR SINGULARITY EXTRACTION

Expression (39) and its derivatives can be integrated analytically over a cuboid volume using the formulas

$$\int_{x_1}^{x_2}\int_{y_1}^{y_2}\int_{z_1}^{z_2}\frac{1}{R_{\pm}}\mathrm{d}x\mathrm{d}y\mathrm{d}z = \Bigg[\Bigg[\Bigg[xy\log(R_{\pm}+z) + xz\log(R_{\pm}+y) + yz\log(R_{\pm}+x) - \frac{1}{2}\left(x^2\tan^{-1}\left(\frac{yz}{xR_{\pm}}\right) + y^2\tan^{-1}\left(\frac{xz}{yR_{\pm}}\right) + z^2\tan^{-1}\left(\frac{xy}{zR_{\pm}}\right)\right)\Bigg]_{x_1}^{x_2}\Bigg]_{y_1}^{y_2}\Bigg]_{z_1}^{z_2}$$

$$\int_{x_1}^{x_2}\int_{y_1}^{y_2}\int_{z_1}^{z_2}\frac{\partial^2}{\partial x^2}\frac{1}{R_{\pm}}\mathrm{d}x\mathrm{d}y\mathrm{d}z = -\Bigg[\Bigg[\Bigg[\tan^{-1}\left(\frac{yz}{xR_{\pm}}\right)\Bigg]_{x_1}^{x_2}\Bigg]_{y_1}^{y_2}\Bigg]_{z_1}^{z_2}$$

$$\int_{x_1}^{x_2}\int_{y_1}^{y_2}\int_{z_1}^{z_2}\frac{\partial^2}{\partial x\partial y}\frac{1}{R_{\pm}}\mathrm{d}x\mathrm{d}y\mathrm{d}z = \Bigg[\Bigg[\Bigg[\log(R_{\pm}+z)\Bigg]_{x_1}^{x_2}\Bigg]_{y_1}^{y_2}\Bigg]_{z_1}^{z_2}, \tag{C1}$$

with the latter two integrals known from geomagnetic modelling (Bhattacharyya 1964). The first and third antiderivative are smooth over the volume. Thus, the definite integrals have limiting value zero for $V \to 0$. The integrand in the second line, however, must be regarded as a generalized function, which can be seen from inspection of the Poisson equation for a point source known from potential theory (e.g. Blakely 1995)

$$\nabla^2 f(\mathbf{r}) = -4\pi\delta(\mathbf{r}-\mathbf{r}') \tag{C2}$$

when the solution $f = \frac{1}{R_{-}}$ is substituted. The inverse tangent is a continuous function throughout the volume as long as the singularity at $R_{-} = 0$ is not included. If, however, the singularity is within the volume, a discontinuity occurs that accounts for the fact that even for an infinitesimal volume the integral does not vanish. For a finite cube with symmetric extension around the singular point $-\epsilon < \{x, y, z\} < \epsilon$, we find the value

$$\Bigg[\Bigg[\Bigg[\tan^{-1}\left(\frac{yz}{xR_{-}}\right)\Bigg]_{-\epsilon}^{\epsilon}\Bigg]_{-\epsilon}^{\epsilon}\Bigg]_{-\epsilon}^{\epsilon} = \sum_{i=1,2}\sum_{j=1,2}\sum_{k=1,2}(-1)^{i+j+k}\tan^{-1}\left(\frac{(-1)^{i+j+k}}{\sqrt{3}}\right) = \frac{4}{3}\pi, \tag{C3}$$

which is independent of $\epsilon$ and thus also valid for an infinitesimal volume. Consequently, it must be the value coming from the singularity itself. It is identical to the value given by van Bladel (1961) and also to the value obtained from integrating one third of eq. (C2) over this cube. This indicates that the antiderivative is correct.

For a singularity removal technique of this kind with basis functions other than pulse basis functions, the integrals (C1) may not be readily available. At least for polynomial basis functions, the homogeneity of the integrands can in principle be exploited as described by Vijayakumar & Cormack (1988) to find numerical approximations.

## APPENDIX D: MAGNETIC GREEN'S TENSOR OVER A HOMOGENEOUS HALF-SPACE

The elements of the magnetic kernel matrix $\mathbf{K}_M$ are obtained as volume integrals over subsurface blocks of the magnetic Green's tensor $\mathbf{M}(\mathbf{r}'|\mathbf{r})$ as defined in eq. (14). The integration is over the coordinate of the electric source $\mathbf{r}'$, the observer position for the magnetic field $\mathbf{r}$ is in the air-plane above the surface of the Earth. Therefore, the TM-mode components are identically zero. The TE-mode components are also easily deduced by the formalism given by Weidelt (1975). They are

$$M_{xx} = \frac{i}{\omega\mu_0}\frac{1}{2\pi}\frac{(x-x')(y-y')}{r^2}\left(Q_0 - \frac{2}{r}Q_1\right) \tag{D1}$$

$$M_{xy} = -\frac{i}{\omega\mu_0}\frac{1}{2\pi}\left[\left(\frac{2}{r}\frac{(y-y')^2}{r^2} - \frac{1}{r}\right)Q_1 - \frac{(y-y')^2}{r^2}Q_0\right] \tag{D2}$$

$$M_{xz} = \frac{i}{\omega\mu_0}\frac{1}{2\pi}\frac{y-y'}{r}Q_2 \tag{D3}$$

$$M_{yx} = \frac{i}{\omega\mu_0}\frac{1}{2\pi}\left[\left(\frac{2}{r}\frac{(x-x')^2}{r^2} - \frac{1}{r}\right)Q_1 - \frac{(x-x')^2}{r^2}Q_0\right] \tag{D4}$$

$$M_{yy} = -M_{xx} \tag{D5}$$

$$M_{yz} = -\frac{i}{\omega\mu_0}\frac{1}{2\pi}\frac{x-x'}{r}Q_2 \tag{D6}$$

for a flight height $h = -z \leq 0$. Analytic expressions for the Hankel integrals

$$Q_0 = \int_0^\infty \frac{\kappa^2}{\alpha+\kappa}\mathrm{e}^{-\alpha z'+\kappa z}J_0(\kappa r)\mathrm{d}\kappa \tag{D7}$$

$$Q_1 = \int_0^\infty \frac{\kappa}{\alpha+\kappa}\mathrm{e}^{-\alpha z'+\kappa z}J_1(\kappa r)\mathrm{d}\kappa \tag{D8}$$

$$Q_2 = \int_0^\infty \frac{\kappa^2}{\alpha+\kappa}\mathrm{e}^{-\alpha z'+\kappa z}J_1(\kappa r)\mathrm{d}\kappa \tag{D9}$$

have only been found directly on the surface where $\exp\kappa z = 1$. Therefore, a numerical filtering technique (Christensen 1990) is used for calculating the Hankel transform at specified radial distances and depth coordinates. The integration is then performed using a cubic spline interpolant through the discrete output values of the Hankel transform, which is then evaluated as required by the numerical quadrature in Cartesian space.

## APPENDIX E: GRADIENT CALCULATION USING THE ADJOINT METHOD

Here, we give a summarized derivation of the gradient of the objective function computed using the adjoint method. For further details, the reader is encouraged to consult for example Plessix (2006); Pankratov & Kuvshinov (2010) or Egbert & Kelbert (2012).

For simplicity, we derive the gradient with respect to the anomalous conductivity values $\sigma_a$, contained in the vector $\hat{\mathbf{m}}$. The gradient with respect to $\mathbf{m}$ is then obtained by a linear transformation that involves the Jacobian matrix $\frac{\partial\hat{\mathbf{m}}}{\partial\mathbf{m}}$ of the inversion of the logarithmic transform (4).

For any earth model $\hat{\mathbf{m}}$, the electric field fulfils the discretized integral eq. (16), acting as the physical constraint

$$\mathbf{f}(\hat{\mathbf{m}}, \mathbf{E}(\hat{\mathbf{m}})) = \mathbf{A}(\hat{\mathbf{m}})\mathbf{E}(\hat{\mathbf{m}}) - \mathbf{E}_p = \mathbf{0}, \tag{E1}$$

which is linear in $\mathbf{E}$. The objective function $\Phi$ of the inverse problem is augmented to

$$\mathcal{L}(\mathbf{E}(\hat{\mathbf{m}}), \overline{\mathbf{E}}(\hat{\mathbf{m}}), \hat{\mathbf{m}}, \lambda, \overline{\lambda}) = \Phi(\mathbf{E}(\hat{\mathbf{m}}), \overline{\mathbf{E}}(\hat{\mathbf{m}}), \hat{\mathbf{m}}) - \lambda^\dagger\mathbf{f}(\mathbf{E}(\hat{\mathbf{m}}), \hat{\mathbf{m}}) - \overline{\lambda^\dagger\mathbf{f}(\mathbf{E}(\hat{\mathbf{m}}), \hat{\mathbf{m}})}. \tag{E2}$$

Here, $\lambda$ is a vector of complex-valued Lagrange multipliers, which is arbitrary, because $\mathbf{f} = \mathbf{0}$ for all feasible $\mathbf{E}$. The last summand ensures that $\mathcal{L}$ is always real-valued. The additional introduction of dependencies on the complex conjugates $\overline{\mathbf{E}}$ and $\overline{\lambda}$ is a purely formal method of the so-called 'Wirtinger calculus' (Remmert 1991) in order to deal with the complex differentiation of the non-holomorphic functions $\mathcal{L}$ and $\Phi$. As a holomorphic function, $\mathbf{f}$ has by definition no formal dependency on $\overline{\mathbf{E}}$, while $\overline{\mathbf{f}}$ has no dependency on $\mathbf{E}$.

The perturbation $\delta\mathcal{L}$ of $\mathcal{L}$ caused by a small change $\delta\hat{\mathbf{m}}$ in $\hat{\mathbf{m}}$ is identical to the perturbation $\delta\Phi$ of $\Phi$, which we require to construct the gradient. It reads

$$\delta\mathcal{L} = \left[\frac{\partial\Phi(\mathbf{E}, \overline{\mathbf{E}}, \hat{\mathbf{m}})}{\partial\hat{\mathbf{m}}} - \lambda^\dagger\frac{\partial\mathbf{f}(\mathbf{E}, \hat{\mathbf{m}})}{\partial\hat{\mathbf{m}}} - \overline{\lambda}^\dagger\frac{\partial\overline{\mathbf{f}}(\overline{\mathbf{E}}, \hat{\mathbf{m}})}{\partial\hat{\mathbf{m}}} + \left(\frac{\partial\Phi(\mathbf{E}, \overline{\mathbf{E}}, \hat{\mathbf{m}})}{\partial\mathbf{E}} - \lambda^\dagger\frac{\partial\mathbf{f}(\mathbf{E}, \hat{\mathbf{m}})}{\partial\mathbf{E}}\right)\frac{\partial\mathbf{E}(\hat{\mathbf{m}})}{\partial\hat{\mathbf{m}}} + \left(\frac{\partial\Phi(\mathbf{E}, \overline{\mathbf{E}}, \hat{\mathbf{m}})}{\partial\overline{\mathbf{E}}} - \overline{\lambda}^\dagger\frac{\partial\overline{\mathbf{f}}(\overline{\mathbf{E}}, \hat{\mathbf{m}})}{\partial\overline{\mathbf{E}}}\right)\frac{\partial\overline{\mathbf{E}}(\hat{\mathbf{m}})}{\partial\hat{\mathbf{m}}}\right]\delta\hat{\mathbf{m}}. \tag{E3}$$

Here, the notation $\mathbf{E}$ [as opposed to $\mathbf{E}(\hat{\mathbf{m}})$] is used to express formal independence of $\mathbf{E}$ from $\hat{\mathbf{m}}$ (during differentiation). With $\partial_{\mathbf{E}}\mathbf{f}(\mathbf{E}, \hat{\mathbf{m}}) = \mathbf{A}$ and $\partial_{\overline{\mathbf{E}}}\overline{\mathbf{f}}(\overline{\mathbf{E}}, \hat{\mathbf{m}}) = \overline{\mathbf{A}}$ and because of $\partial_{\mathbf{E}}\Phi(\mathbf{E}, \overline{\mathbf{E}}, \hat{\mathbf{m}}) = \partial_{\overline{\mathbf{E}}}\Phi(\mathbf{E}, \overline{\mathbf{E}}, \hat{\mathbf{m}})$, it can easily be verified that a choice of $\lambda$, such that

$$\mathbf{A}^\dagger\lambda = \left(\frac{\partial\Phi(\mathbf{E}, \overline{\mathbf{E}}, \hat{\mathbf{m}})}{\partial\mathbf{E}}\right)^\dagger \tag{E4}$$

is satisfied, leads to a cancellation of the terms within both parenthesis in eq. (E3). Thus, with a solution $\lambda$ to the adjoint system (E4), the gradient follows from the remaining terms

$$\nabla_{\hat{\mathbf{m}}}\Phi = \nabla_{\hat{\mathbf{m}}}\mathcal{L} = \left(\frac{\partial\Phi(\mathbf{E}, \overline{\mathbf{E}}, \hat{\mathbf{m}})}{\partial\hat{\mathbf{m}}} - 2\mathcal{R}\left[\lambda^\dagger\frac{\partial\mathbf{f}(\mathbf{E}, \overline{\mathbf{E}}, \hat{\mathbf{m}})}{\partial\hat{\mathbf{m}}}\right]\right)^T, \tag{E5}$$

where $\mathcal{R}(z) = \frac{1}{2}(z+\bar{z})$ denotes the real part of $z$.

In the following, the forms of the derivatives in the eqs (E4) and (E5) are given explicitly. The magnetic transfer functions $\mathbf{t}$ are uniquely determined from two plane wave polarizations (1 and 2):

$$\mathbf{g}(\mathbf{E}_1, \mathbf{E}_2, \hat{\mathbf{m}}) = \mathbf{t}(\mathbf{H}_1(\mathbf{E}_1, \hat{\mathbf{m}}), \mathbf{H}_2(\mathbf{E}_2, \hat{\mathbf{m}})) = \begin{bmatrix}\mathbf{t}_x\\ \mathbf{t}_y\end{bmatrix} = \begin{bmatrix}\frac{\Delta(\mathbf{H}_z, \mathbf{H}_y)}{\Delta(\mathbf{H}_x, \mathbf{H}_y)}\\ \frac{\Delta(\mathbf{H}_z, \mathbf{H}_x)}{\Delta(\mathbf{H}_y, \mathbf{H}_x)}\end{bmatrix}$$

$$[\Delta(\mathbf{A}, \mathbf{B})]_k = A_{1,k}B_{2,k} - A_{2,k}B_{1,k}. \tag{E6}$$

Consequently, the forward calculation $\mathbf{g}$ contains two differently polarized electromagnetic fields that satisfy $\mathbf{f}_{\{1,2\}}$ with two different primary fields $\mathbf{E}_{p,\{1,2\}}$. Each of them comes with an independent set of Lagrange multipliers and an independent adjoint problem. Consequently, we will have to solve two independent adjoint equations to compute the gradient.

We obtain the derivatives with respect to $\hat{\mathbf{m}}$ and with respect to the electric fields

$$\frac{\partial\Phi(\mathbf{E}_1, \overline{\mathbf{E}}_1, \mathbf{E}_2, \overline{\mathbf{E}}_2, \hat{\mathbf{m}})}{\partial\hat{\mathbf{m}}} = 2\mathcal{R}\left[\left(\mathbf{g}(\hat{\mathbf{m}}) - \mathbf{d}^{\mathrm{obs}}\right)^\dagger(\partial_{\hat{\mathbf{m}}}\mathbf{g})\right]$$

$$\frac{\partial\Phi(\mathbf{E}_1, \overline{\mathbf{E}}_1, \mathbf{E}_2, \overline{\mathbf{E}}_2, \hat{\mathbf{m}})}{\partial\mathbf{E}_{\{1,2\}}} = \left(\mathbf{g}(\hat{\mathbf{m}}) - \mathbf{d}^{\mathrm{obs}}\right)^\dagger(\partial_{\mathbf{E}_{\{1,2\}}}\mathbf{g}). \tag{E7}$$

The Fréchet derivatives read

$$\partial_{\hat{\mathbf{m}}}\mathbf{g}(\mathbf{E}_1, \mathbf{E}_2, \hat{\mathbf{m}}) = \partial_{\mathbf{H}_1}\mathbf{t}\partial_{\hat{\mathbf{m}}}\mathbf{H}_1 + \partial_{\mathbf{H}_2}\mathbf{t}\partial_{\hat{\mathbf{m}}}\mathbf{H}_2$$

$$\partial_{\mathbf{E}_1}\mathbf{g}(\mathbf{E}_1, \mathbf{E}_2, \hat{\mathbf{m}}) = \partial_{\mathbf{H}_1}\mathbf{t}\partial_{\mathbf{E}_1}\mathbf{H}_1$$

$$\partial_{\mathbf{E}_2}\mathbf{g}(\mathbf{E}_1, \mathbf{E}_2, \hat{\mathbf{m}}) = \partial_{\mathbf{H}_2}\mathbf{t}\partial_{\mathbf{E}_2}\mathbf{H}_2, \tag{E8}$$

where $\partial_{\mathbf{H}_1}\mathbf{t}$ and $\partial_{\mathbf{H}_2}\mathbf{t}$ each are block-diagonal matrices of the form

$$\partial_{\mathbf{H}_{\{1,2\}}}\mathbf{t} = \begin{bmatrix}\partial_{\mathbf{H}_{x,\{1,2\}}}\mathbf{t}_x & \partial_{\mathbf{H}_{y,\{1,2\}}}\mathbf{t}_x & \partial_{\mathbf{H}_{z,\{1,2\}}}\mathbf{t}_x\\ \partial_{\mathbf{H}_{x,\{1,2\}}}\mathbf{t}_y & \partial_{\mathbf{H}_{y,\{1,2\}}}\mathbf{t}_y & \partial_{\mathbf{H}_{z,\{1,2\}}}\mathbf{t}_y\end{bmatrix}. \tag{E9}$$

Together, the latter comprise the matrix

$$\mathbf{T} := \begin{bmatrix} \partial_{\mathbf{H}_1}\mathbf{t}_x & \partial_{\mathbf{H}_2}\mathbf{t}_x \\ \partial_{\mathbf{H}_1}\mathbf{t}_y & \partial_{\mathbf{H}_2}\mathbf{t}_y \end{bmatrix} = \begin{bmatrix} \mathbf{T}_1 & \mathbf{T}_2 \end{bmatrix}. \tag{E10}$$

Furthermore,

$$\partial_{\hat{\mathbf{m}}}\mathbf{H}_{\{1,2\}} = \mathrm{i}\omega\mu\mathbf{K}_M\mathbf{D}_{\mathbf{III},\{1,2\}} \tag{E11}$$

with

$$\mathbf{D}_{\mathbf{III},\{1,2\}} = \begin{bmatrix} \mathrm{diag}(\mathbf{E}_{\{1,2\},x}) \\ \mathrm{diag}(\mathbf{E}_{\{1,2\},y}) \\ \mathrm{diag}(\mathbf{E}_{\{1,2\},z}) \end{bmatrix}, \tag{E12}$$

where $\mathrm{diag}(\mathbf{x})$ is a diagonal matrix with the vector $\mathbf{x}$ on its diagonal. Additionally,

$$\partial_{\mathbf{E}_{\{1,2\}}}\mathbf{H}_{\{1,2\}} = \mathbf{K}_M\Sigma \tag{E13}$$

and

$$\partial_{\hat{\mathbf{m}}}\mathbf{f} = \partial_{\hat{\mathbf{m}}}\mathbf{A}(\hat{\mathbf{m}}) \cdot \mathrm{diag}(\mathbf{E}_{\{1,2\}}) = \mathrm{i}\omega\mu\mathbf{K}\mathbf{D}_{\mathbf{III},\{1,2\}}. \tag{E14}$$

The adjoint systems are then

$$\mathbf{A}^\dagger\lambda_{\{1,2\}} = -\Sigma\mathbf{K}_M^\dagger\mathbf{T}_{\{1,2\}}^\dagger\left(\mathbf{g}(\hat{\mathbf{m}}) - \mathbf{d}^{\mathrm{obs}}\right) \tag{E15}$$

and the gradient reads

$$\nabla_{\hat{\mathbf{m}}}\Phi = 2\mathcal{R}\left\{\mathrm{i}\omega\mu\left[\left(\mathbf{g}(\hat{\mathbf{m}}) - \mathbf{d}^{\mathrm{obs}}\right)^\dagger\mathbf{T}\begin{bmatrix}\mathbf{K}_M & \\ & \mathbf{K}_M\end{bmatrix} - \begin{bmatrix}\lambda_1 \\ \lambda_2\end{bmatrix}^\dagger\begin{bmatrix}\mathbf{K} & \\ & \mathbf{K}\end{bmatrix}\right]\cdot\begin{bmatrix}\mathbf{D}_{\mathbf{III},1} \\ \mathbf{D}_{\mathbf{III},2}\end{bmatrix}\right\}^T. \tag{E16}$$